Chinese Chemical Letters 37 (2026) 112689

Contents lists available at ScienceDirect

Chinese Chemical Letters

journal homepage: www.elsevier.com/locate/cclet

Advancements in electrocatalytic nitrogen reduction to ammonia

Jie Hou, Bin Liu*, Wenjing Zheng*, Yaling Wang, Guangqun Cao, Shengliang Hu

School of Energy and Power Engineering, State Key Laboratory of Coal and CBM Co-Mining, North University of China, Taiyuan 030051, China

ARTICLE INFO

Article history:
Received 24 December 2025
Revised 17 March 2026
Accepted 26 March 2026
Available online 27 March 2026

Keywords:
Electrocatalysis
Nitrogen reduction reaction
Catalyst
Catalytic mechanisms
Detection methods

ABSTRACT

The electrochemical nitrogen reduction reaction (NRR) is widely regarded as a promising sustainable alternative to the energy-intensive Haber-Bosch process for ammonia synthesis. In recent years, a large number of studies have focused on enhancing key NRR performance metrics, particularly Faradaic efficiency and ammonia (NH_3) yield rate, leading to notable progress in both areas. Despite these advances, the development of low-cost, high-performance electrocatalysts remains the primary challenge and a major bottleneck to large-scale industrial application. This review summarizes the current understanding of NRR mechanisms and reaction pathways, as well as recent progress in electrochemical cell design, quantitative NH_3 detection strategies, and electrocatalyst development. Focusing on electrocatalysts, we provide an overview of the major classes of electrocatalysts including noble metals, transition metals, single-atom systems, metal-organic frameworks, and non-metallic materials. Furthermore, we compare their respective advantages and limitations. Finally, we outline the key challenges and future directions for engineering next-generation electrocatalysts capable of achieving high-efficiency nitrogen fixation.

© 2026 Published by Elsevier B.V. on behalf of Chinese Chemical Society and Institute of Materia Medica, Chinese Academy of Medical Sciences.

1. Introduction

NH_3 is a vital clean energy material with widespread applications in fertilizer production, explosives manufacturing, steelmaking, and other industrial fields [1]. In nature, NH_3 is primarily produced through biological nitrogen fixation and high-energy nitrogen fixation [2]. Biological nitrogen fixation involves microorganisms converting atmospheric N_2 into NH_3, facilitated by the nitrogenase enzyme complex, which significantly lowers the energy barrier for the reduction of N_2 [3]. However, this process is extremely slow due to stringent environmental requirements and the enzyme's high demands. Similarly, high-energy nitrogen fixation during thunderstorms uses lightning energy to convert atmospheric N_2 and H_2O into NH_3 [4]. However, the resulting NH_3 is difficult to capture and unsuitable for industrial-scale production. Given these limitations in natural pathways, significant research focus has shifted to artificial nitrogen fixation techniques, particularly the Haber-Bosch process (H-B), photocatalysis, and electrocatalysis [5–7].

Despite these emerging alternatives, industrial NH_3 synthesis remains overwhelmingly dependent on the century-old H-B method. This method requires extreme operating conditions (300–500 °C, 150–200 atm) to activate kinetically inert N_2 molecules. Such thermocatalytic synthesis not only requires capital-intensive infrastructure to maintain these harsh environments but also accounts for approximately 1%–2% of global energy consumption [8]. To address these drawbacks, research calls for alternative methods capable of producing NH_3 under mild conditions. In pursuit of sustainable solutions, electrochemical and photochemical approaches coupled with renewable energy utilization are increasingly explored for NRR [9]. Among these approaches, photocatalytic N_2 fixation faces limitations including solar energy's intermittency and low conversion efficiency, resulting in low NH_3 yields. Compounding these issues, stringent bandgap requirements for semiconductor catalysts further constrain its practicality. Consequently, the NRR *via* electrocatalysis holds distinct advantages over photocatalytic methods [10,11]. Specifically, electric energy, as a renewable resource, facilitates an eco-friendly and sustainable process. Electrocatalysis not only achieves higher NH_3 yields but also maximizes catalyst utilization by precisely controlling reaction temperature and applied potential [12]. In recent years, research on electrocatalysts for the NRR has evolved from macroscopic to microscopic scales and from theoretical exploration to practical application [13]. In the early stages (around the beginning of the 2010s), studies primarily focused on bulk metals and metal oxides, which verified the theoretical feasibility of NRR but often suffered from low catalytic efficiency. From approximately 2015 onward, research attention shifted to the regulation of nanostructures and morphologies [14]. By constructing nano- and porous structures to increase the density of active sites, the yield was improved, though

* Corresponding authors.
E-mail addresses: liubin@nuc.edu.cn (B. Liu), wenjingzheng@nuc.edu.cn (W. Zheng).

https://doi.org/10.1016/j.cclet.2026.112689
1001-8417/© 2026 Published by Elsevier B.V. on behalf of Chinese Chemical Society and Institute of Materia Medica, Chinese Academy of Medical Sciences.

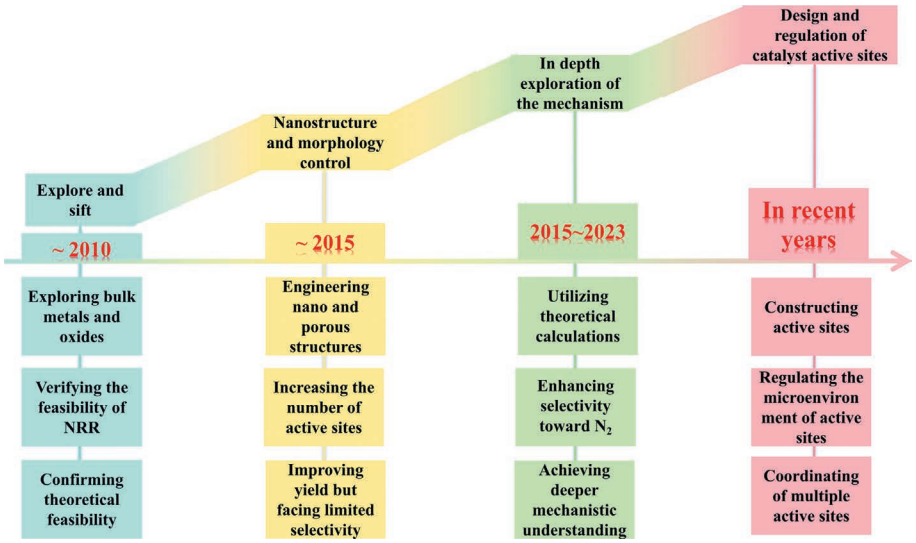


Fig. 1. The evolution of the NRR development.

challenges in selectivity persisted. Since 2023, NRR research has further advanced to the precise design and regulation of catalytic active sites, including strategies such as active-site construction, microenvironment modulation, and multi-active-site coordination [15]. Meanwhile, theoretical calculations have been integrated to guide defect engineering and deepen the understanding of reaction mechanisms [16–18]. As illustrated in Fig. 1, these advances are driving the development of NRR catalysts towards higher efficiency and selectivity. Nevertheless, despite this progress, electrocatalytic NRR still faces critical challenges, including the intrinsically high energy barrier for N≡N activation, severe competition from the hydrogen evolution reaction (HER), and consequently low Faradaic efficiency (FE) and NH_3 yield [19,20].

To overcome these barriers, comprehensive optimization of the entire system is necessary to achieve high FE and NH_3 yield in electrochemical NRR [21]. Firstly, the rational design of highly active, selective, and stable heterogeneous electrocatalysts constitutes the cornerstone for efficient ambient-condition N_2 to NH_3 conversion. Secondly, a fundamental understanding of NRR pathways and mechanisms is crucial for enhancing catalytic efficiency. Finally, the design of electrolytic cells and methods for NH_3 quantification detection significantly influences accurate assessment and overall process effectiveness.

Accordingly, this review aims to address these challenges by systematically summarizing recent advances in NRR pathways, electrolytic cells, NH_3 detection methods, and catalyst design strategies.

2. Reaction pathways of NRR

The reaction pathways for the electrochemical reduction of N_2 to NH_3 can be classified into two categories: the dissociative pathway and the associative pathway [22]. In the dissociative pathway, the N≡N triple bond is cleaved prior to hydrogenation of nitrogen atoms (Fig. 2a). Because the bond energy of N≡N is very high, it limits the reaction kinetics to a certain extent. Therefore, it is rather difficult to carry out the dissociative pathway at normal temperature and pressure. The H-B method adopts this pathway, which is why it requires such harsh conditions. In contrast, the associative pathway involves the simultaneous breaking of the N–N bond and release of the first NH_3 molecule [23,24].

It can be further subdivided into distal and alternating pathways based on the hydrogenation sequence (Fig. 2b) [8,25]. In the distal pathway, the terminal N atom is hydrogenated first and released as NH_3 ($^*N_2 \rightarrow {}^*NNH \rightarrow {}^*NNH_2 \rightarrow N + NH_3$). The remaining surface-bound N then undergoes reductive hydrogenation to yield a second NH_3 molecule ($N \rightarrow {}^*NH \rightarrow {}^*NH_2 \rightarrow {}^*NH_3 \rightarrow NH_3$). In the alternating pathway, reductive hydrogenation occurs alternately at the distal and proximal N atoms, and the two NH_3 molecules are released sequentially at the final stages ($^*N_2 \rightarrow {}^*NNH \rightarrow {}^*NHNH \rightarrow {}^*NHNH_2 \rightarrow {}^*NH_2NH_2 \rightarrow {}^*NH_2NH_3 \rightarrow {}^*NH_2 + NH_3$; $^*NH_2 \rightarrow {}^*NH_3 \rightarrow NH_3$). However, as a biologically inspired reaction pathway, the enzymatic pathway differs from the traditional associative pathway (Fig. 2c), primarily in the adsorption mode of the N_2: The molecule adsorbs transversely between two active sites on the catalyst surface, thereby facilitating subsequent hydrogenation [26,27].

Currently, numerous researchers have elucidated the reaction pathways involved in the NRR process through extensive experiments and theoretical simulations, and revealed that the preferred pathway is critically dependent on the specific catalyst systems employed. For example, He *et al.* developed a metal-organic framework catalyst [PCN-222(Fe)] and systematically explored the NRR catalytic pathways by means of density functional theory (DFT) [28]. As shown the Gibbs free-energy diagram in Fig. 2d, the alternating pathway exhibits a lower reaction energy barrier than that of the distal pathway, thereby establishing it as the dominant mechanism. Similarly, Zhang *et al.* employed non-noble metal-based hollow carbon spheres embedded with VO_2 for electrocatalytic NRR [29], achieving both high stability and superior NH_3 yield. The catalyst exhibits excellent selectivity through the alternating pathway, and UV–vis spectrophotometry detected no N_2H_4 by-product in the reaction electrolyte (Fig. 2e). However, some catalytic systems employed a distal pathway. For example, Lai *et al.* developed metal vacancy-rich sub-boron nanosheets that delivered an exceptional FE of 66.7 % [21]. *In situ* Fourier-transform infrared (FTIR) spectroscopy revealed a strong preference for the distal pathway on the sub-boron surface. Further mechanistic insights were gained through DFT calculations, which quantified the reaction energies and Gibbs free energy changes of key intermediates. The rate-determining step (RDS) for the distal pathway exhibited a lower energy barrier (+0.60 eV) than that for the alternating pathway (+0.91 eV). Recently, Cheng *et al.* successfully fabricated FeS_2−MBene composites [30]. The S-modified structure significantly increases the charge density around the Mo active sites. The constructed electron-rich interface optimized the distal pathway by reducing the adsorption energy of the $^*N$–NH_2 inter-

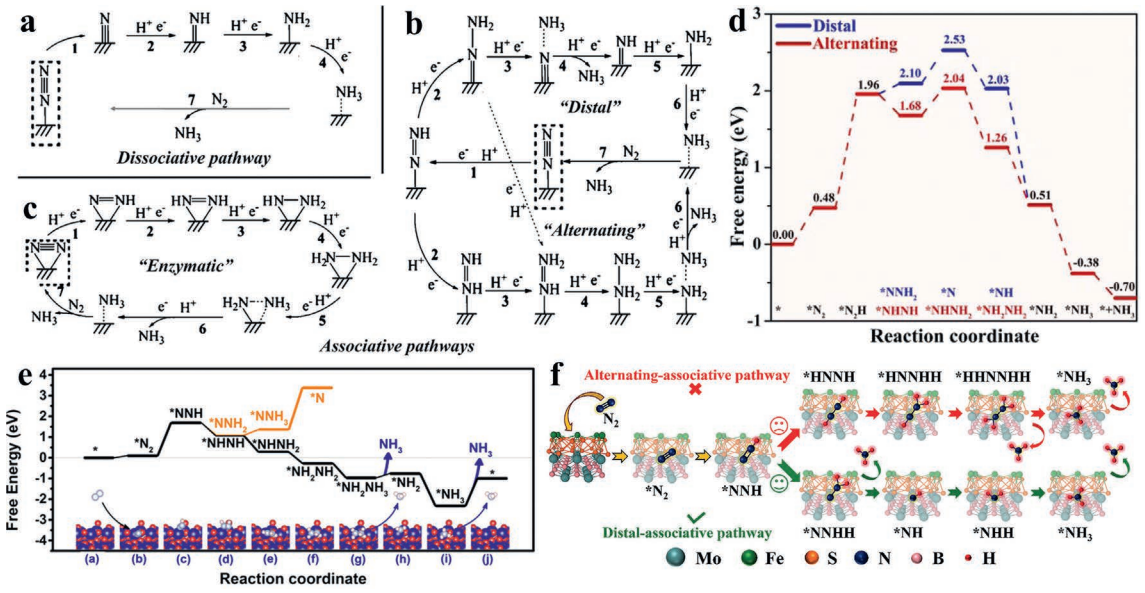


Fig. 2. (a) Schematic diagram of the dissociation pathways of NRR. (b) Schematic diagram of the distal and alternating pathways of NRR. (c) Schematic diagram of the enzymatic pathway of NRR. Reproduced with permission [25]. Copyright 2018, Elsevier. (d) Free-energy profile for the NRR process on a PCN-222(Fe). Reproduced with permission [28]. Copyright 2022, Elsevier. (e) Free-energy profile for the NRR process on a VO_2 (211) surface. The asterisk (*) denotes the adsorption site. Reproduced with permission [29]. Copyright 2019, Wiley-VCH Verlag GmbH & Co. KGaA, Weinheim. (f) Schematic illustration of the distal-associative pathway over FeS_2−MBene for the catalytic conversion of N_2 to NH_3. Reproduced with permission [30]. Copyright 2024, Wiley-VCH GmbH.

mediate, thereby preventing active site blockage caused by overly strong adsorption, as shown in Fig. 2f.

In summary, the electrocatalytic N_2 reduction pathway varies significantly across catalyst systems. Although the three generally recognized reaction pathways are widely accepted, the NRR mechanism still requires further investigation due to the continuously evolving reaction intermediates during the throughout the catalytic process. Currently, the limited understanding of the true active sites and key reaction steps means that catalyst development largely relies on trial and error. Establishing a clear correlation between specific active sites and their corresponding reaction pathways across different catalyst systems would enable a more comprehensive understanding of NRR mechanisms and provide rational guidance for future catalyst design.

3. Electrolytic cells of NRR

Currently, various electrochemical cells have been developed for NRR-driven NH_3 synthesis, including single-chamber, H-type, flow, gas circulation, pressurized electrochemical, and gas diffusion electrode cell (GDE electrolytic cell) [25,31,32]. Below, we discuss the advantages and limitations of each of these cells and summarized them in Table 1.

For the widely used H-type cell, it comprises two glass compartments connected by a porous separator (*e.g.*, Nafion membrane), with the working and counter electrodes placed in separate chambers (Fig. 3a) [33,34]. Its simple geometry facilitates assembly and operation. However, the Nafion membrane cannot completely prevent the permeation of NH_4^+ between the anode and cathode, which leads to the crossover of NH_3/NH_4^+ in the cell. This phenomenon leads to an underestimation of the NH_3 production rate [25].

Unlike H-type cell, the cathode and anode of single-chamber electrolytic cell are placed in the same chamber, as shown in Fig. 3b [25,35]. This cell faces severe HER and low N_2 solubility, restricting NRR efficiency and further leading to consistently low FE. Furthermore, O_2 generated at the anode and NH_3 from cathode product are easily diffuse freely throughout the cell. In this case, O_2 will suppress the cathodic N_2 reduction reaction and NH_3 may be oxidized at the anode, leading to an underestimation of the actual NH_3 production activity [23,36]. Therefore, this type of cell has no practical application value.

To address the mass transfer problems inherent to H-type and single-chamber electrolytic cells, flow cells have been developed (Fig. 3c). In a flow cell, the electrolyte passes over the electrode surfaces, promoting rapid reactant delivery and enabling high reaction rates, which makes this configuration particularly suitable for high-current-density applications [37]. Flow cells can also suppress the HER by restricting the proton availability on the cathode catalyst. However, the cathode surface must remain wetted under catalytic conditions, and the low-overpotential HER is still unavoidable. Consequently, the selectivity toward N_2 reduction remains insufficient and requires further improvement [38].

The gas circulation cell is an enhanced version of the H-type cell, achieved by continuously bubbling and circulating N_2 gas through the electrolyte (Fig. 3d). This modification increases local N_2 concentration near the electrode surface, thereby improving electrochemical performance to some extent. Nevertheless, the enhancement remains limited, as this strategy does not fundamentally overcome the intrinsic mass transfer limitations associated with gaseous reactants and also introduces additional operational complexity [39].

Pressurized electrolytic cells offer another enhancement strategy by applying elevated pressure to systems such as H-type or flow cells (Fig. 3e). Increasing system pressure enhances N_2 solubility in the electrolyte, which significantly improves electrochemical performance [40]. This approach provides a generalizable solution to dissolution-related mass transfer limitations across multiple cell configurations. However, it requires stringent equipment sealing and high safety standards, inevitably increasing energy consumption and overall cost.

The polymer electrolyte membrane (PEM-type cell) employs a Nafion membrane to separate the cathode and anode compartments. N_2 is fed to the cathode, while the anode contains a liquid electrolyte, forming a "gas-solid-liquid" three-phase interface that offers exceptionally high gas mass transfer efficiency, as shown

Table 1
Comparison of different electrolytic cells for NRR.

Categories		Features	Advantages	Disadvantages
Traditional electrolytic cells	H-type cell	Two glass compartments connected by a Nafion membrane; Working and counter electrodes in separate chamber	Simple structure; Easy to assemble and operate; Low cost	Low N_2 solubility; NH_3 easily crosses over and is oxidized at the counter electrode
	Single-chamber cell	Working and counter electrodes in the same chamber	Simple structure	Severe product crossover contamination
Enhanced electrolytic cells	Flow cell	Anode fed with electrolyte solution	Mass transfer greatly enhances; Continuous supply of reactants and removal of products	Complex system
	Gas circulation cell	An enhanced H-type cell with a characteristic of circulating N_2 gas in the electrolyte	High N_2 solubility and fast refresh rate	Complex system
	Pressurized cell	An enhanced H-type or flow cell with additional pressure	High N_2 solubility	High standard of equipment sealing and safety
GDE electrolytic cells	PEM-type cell	Gas-solid-liquid three-phase system	High N_2 mass transfer efficiency; Fast reaction rate	Complex system

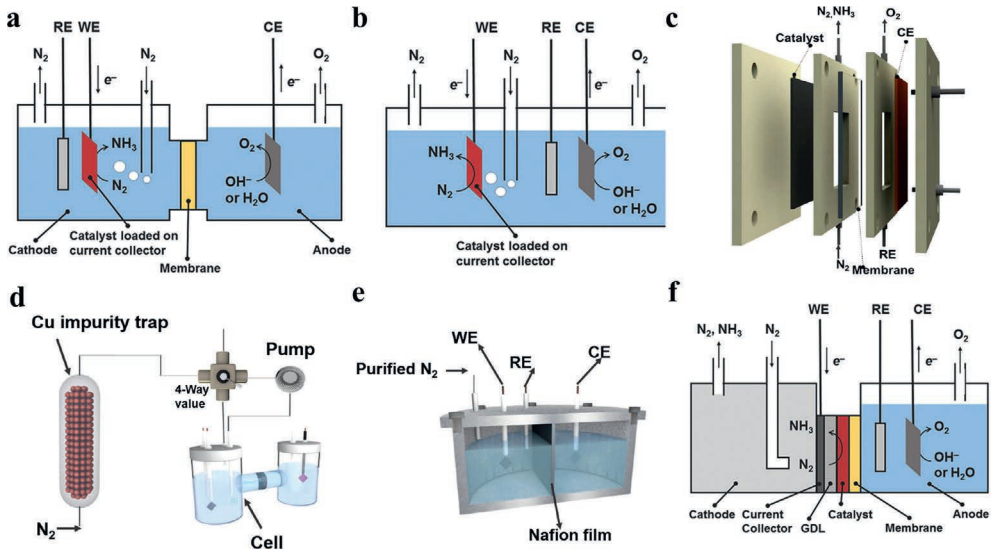


Fig. 3. The schematic diagrams of H-type cell (a), single-chamber electrochemical cell (b), flow cell (c), gas circulation cell (d), pressurized electrochemical cell (e), and PEM-type cell (f). Reproduced with permission [23,25]. Copyright 2018, Wiley-VCH Verlag GmbH & Co. KGaA, Weinheim; Copyright 2023, American Chemical Society.

in Fig. 3f. Compared with conventional solid-state polymer membrane cells, this cell offers two major advantages: it allows the incorporation of a reference electrode for real-time monitoring of the working electrode potential, and the presence of liquid electrolyte ensures sufficient wetting of the Nafion membrane, thereby minimizing conductivity losses. However, the design also suffers from significant NH_3 crossover, causing the detected NH_3 yield to be lower than the actual production [25].

4. Ammonia detection methods of NRR

Accurate detection and quantification of NH_3 is essential for electrocatalytic nitrogen fixation, as various interfering factors may arise during measurement. A variety of analytical techniques are available for NH_3 detection, with the most common being spectrophotometry/colorimetry (*e.g.,* Nessler's reagent method, salicylic acid methods) [41], ion chromatography [42], and ^{15}N isotope-based nuclear magnetic resonance spectroscopy (^{15}N NMR) [43]. In practice, the selection of methods strongly depends on the NH_3 concentration range. At low NH_3 concentrations, many factors (*e.g.,* pH, impurity ions, NH_3-containing molecules, certain catalyst solvents) can interfere with detection. Therefore, selecting a suitable detection method is crucial for obtaining reliable results [44]. This section summarizes the most widely used solution-phase NH_3 quantification methods and compares their advantages and limitations including detection ranges, test environments, characteristics, and precautions in Table 2.

In Nessler's reagent spectrophotometry, iodide and mercury ions coordinate with NH_4^+ under strongly alkaline condition to form a colored complex with a characteristic absorption at 420 nm. The absorbance follows the Lambert-Beer law in the range of 0.025–5.0 mg/L. Although simple to operate, this method involves highly toxic mercury-containing reagents, posing substantial environmental and safety risks. Besides, the reagent suffers from poor stability, and metal ions such as Fe^{2+}, Cu^{2+}, and Ca^{2+} may interfere with the test results [45,46].

For salicylate spectrophotometry method, NH_4^+ reacts sequentially with salicylate, hypochlorite, and sodium nitroprusside to form a blue complex with a characteristic absorption peak at 664 nm. The linear detection range is 0.01–1.0 mg/L. While the reagents exhibit lower toxicity than those used in the Nessler method, the measurement requires a strongly alkaline environment (pH > 11), and the detection range is narrower.

Compared with the above methods, ion chromatography offers high sensitivity, accurate quantification, and rapid analysis, with a broad detection range of 0.02–40 mg/L. But, the NH_4^+ signal can

Table 2
Comparison of different methods for NH_3 determination.

Test method	Detection range of NH_3	Test environment of NH_3	Characteristics	Precautions during the detection process
Nessler's reagent	0.025~5.0 mg/L	Neutral, alkaline and acidic conditions	Easy to operate; Toxic chromogenic agent	Interfered by metal ions and organic compounds; Unstable chromogenic agent
Salicylic acid method	0.01~1.0 mg/L	pH ≥ 11	Easy to operate; Low toxicity	Interfered by Fe^{2+}; Long color development time
Ion chromatography	0.02~2.0 mg/L	pH = 0~14	Good reproducibility; High sensitivity; Short detection time	Interfered by Na^+
^{15}N NMR spectroscopy	5~10 μmol/L	pH ≥ 11	Trace the source of NH_3	Ensure the purity of ^{15}N

be affected by Na^+ owing to peak overlap between the two ions. ^{15}N NMR spectroscopy also provides accurate quantitative analysis and, importantly, enables tracing of the NH_3 origin using isotopic labeling [47]. Other techniques, such as NH_3 ion selective electrodes and fluorescence methods, are available but require specialized expertise and are less commonly used in routine measurements [48,49].

Besides, rigorous control of contamination sources during experiments is crucial for ensuring the accuracy and reliability of NRR results and therefore requires strict attention from both prevention and traceability perspectives. In terms of contamination prevention, the electrolyte should be continuously purged with an inert gas prior to experiments, and all aqueous electrolytes and solvents should be distilled to reduce NH_3 content. In addition, all sample-handling containers must be treated with freshly prepared acidic cleaning solutions or subjected to high-temperature calcination. For nitrogen source tracing, a series of control experiments including nitrogen-free, catalyst-free, and blank substrate tests should be performed. The same samples should also be analyzed using at least two detection methods based on different principles for cross-validation. When needed, ^{15}N NMR spectroscopy can be employed to further trace the nitrogen origin, thereby ensuring the reliability of the experimental data.

5. The main electrocatalysts for NRR

Electrocatalysts play a decisive role in the entire NRR process, governing reaction kinetics, NH_3 yield, and even the reaction pathway. This section highlights recent advances in noble metal, transition metal, single-atom, metal-organic frameworks, and nonmetallic catalysts [50].

5.1. Noble metal catalysts

Noble metals (*e.g.,* Au, Ag, Pd, Pt, Ru, Rh, Os, Ir) are attractive NRR catalysts owing to their high stability, corrosion resistance, and excellent electrical conductivity. However, their high-cost limits large-scale industrial application. To improve activity while mitigating cost, strategies such as engineering morphology, crystallinity, and crystal orientation have been widely adopted to maximize specific surface area, enhance active site density, and improve metal utilization efficiency [51–54].

Au-based catalysts have been extensively investigated due to their favorable catalytic properties. Current strategies focus primarily on tailoring the physical structure of Au and dispersing Au nanoparticles on conductive supports to achieve synergistic enhancement. This is also a common strategy currently adopted in the areas of catalysis and energy storage [55,56]. For example, Wang *et al.* reported flower-like Au microstructures *via* a rapid reduction method (Fig. 4a) [57]. The interconnected nanosheets exposed abundant active sites, accelerating the reaction rate and delivering an NH_3 yield of 25.57 μg h^{-1} mg_{cat}^{-1} with an FE of 6.05 %. Notably, the catalyst showed 100 % selectivity for NRR, and its flower-like architecture doubled the NH_3 yield compared with spherical Au particles. Incorporating Au into other metal matrices provides another effective approach to improve catalysis efficiency. Wang *et al.* constructed Au@SnO_2 nanoparticles with regulated oxygen-vacancy concentrations by using nitrogen-adsorptive ultrathin SnO_2 as a conductive carrier (Fig. 4b) [58]. This catalyst

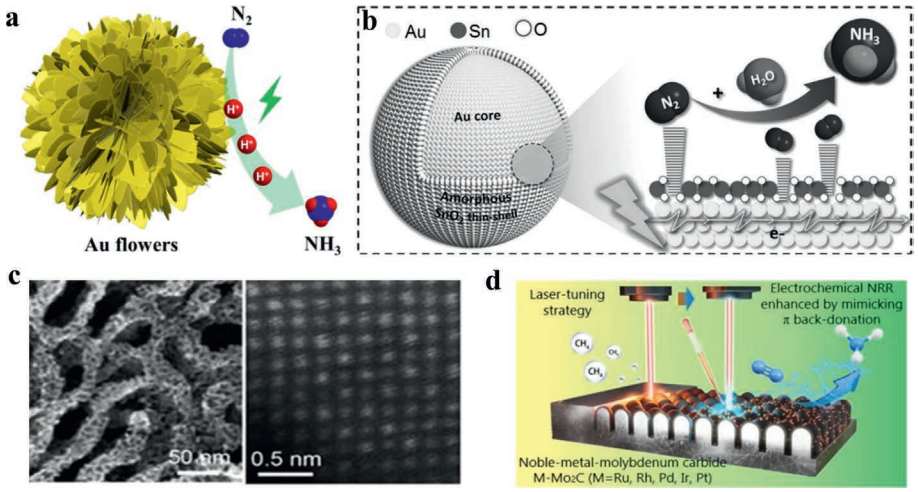


Fig. 4. (a) Schematic diagram of the electrocatalytic reduction of N_2 to NH_3 by Au flower. Reproduced with permission [57]. Copyright 2018, Wiley-VCH Verlag GmbH & Co. KGaA, Weinheim. (b) Schematic diagram of the enhanced type of Au@A-SnO_2NPs/C catalyst. Reproduced with permission [58]. Copyright 2019, Elsevier. (c) SEM image of Pd_3Cu_1. Reproduced with permission [61]. Copyright 2019, Elsevier. (d) Schematic diagram of the electrocatalytic reduction of N_2 to NH_3 by M-Mo_2C. Reproduced with permission [62]. Copyright 2022, Elsevier.

Table 3
Representative types and properties of noble metal catalysts.[a]

Electrocatalyst	Electrolyte	Potential (V *vs.* RHE)	Yield rate of NH_3 ($\mu g\,h^{-1}\,mg_{cat}^{-1}$)	FE (%)	Ref.
Au nanoflower	0.1 mol/L KCl	−0.20	25.57	6.1	[57]
Au@A-SnO_2NPs/C	0.1 mol/L HCl	−0.20	21.90	15.2	[58]
Au np-$MoSe_2$	0.1 mol/L HCl	−0.30	30.83	37.8	[59]
Pd-TA nanoparticles	0.1 mol/L Na_2SO_4	−0.40	24.12	9.5	[60]
Pd_3Cu_1	1.0 mol/L KOH	−0.25	39.90	1.2	[61]
Rh-Mo_2C	0.1 mol/L Na_2SO_4	−0.125/−0.30	26.30 [b]	15.4	[62]
Rh-NNs	0.1 mol/L KOH	−0.20/0.00	23.88 [b]	0.2	[63]

[a] Testing condition: room temperature/atmospheric pressure; N_2 flow rate (about 20 mL/min).
[b] The unit is $\mu g\,h^{-1}\,cm^{-2}$.

achieved an NH_3 yield of 21.9 μg h^{-1} mg_{cat}^{-1} and an FE of 15.2 % at −0.20 V *vs*. RHE. Likewise, Chen *et al*. realized atomic dispersion of Au in np-$MoSe_2$ *via* chemical etching [59], achieving an outstanding NH_3 yield of 30.83 $\mu g\,h^{-1}\,mg_{cat}^{-1}$ and the remarkably FE of 37.82 % at −0.30 V *vs*. RHE. DFT calculations confirmed that atomically dispersed Au sites facilitate N_2 adsorption and effectively suppress HER.

Pd-based materials exhibit similar advantages. Deng *et al*. synthesized oxygen-enriched Pd nanoparticles through tannic acid surface modification [60], forming high surface area nano catalysts with improved intrinsic activity. This catalyst achieved an NH_3 yield was 24.12 μg h^{-1} mg_{cat}^{-1} and an FE of 9.49 % in 0.1 mol/L Na_2SO_4 at −0.45 V *vs*. RHE. Moving from monometallic to bimetallic systems, Pd-based noble metal alloys have also gained prominence. Pang *et al*. fabricated Pd-Cu nanoporous alloys with 3D linked structures and identified Pd_3Cu_1 as the optimal composition [61]. Its larger specific surface area exposed more active sites (Fig. 4c), resulting in an NH_3 yield of 39.9 $\mu g\,h^{-1}\,mg_{cat}^{-1}$ at −0.25 V *vs*. RHE, outperforming many monometallic catalysts.

Beyond Au and Pd, other noble metals have also received attention. For example, Chang *et al*. incorporated noble metal Lewis acid sites into a Mo_2C substrate using a laser-assisted technique [62], effectively simulating π-backbonding to strengthen N_2 activation and lower the hydrogenation energy barriers (Fig. 4d). Among various noble metals, Rh-modified Mo_2C demonstrated exceptional NRR performance, achieving an NH_3 yield of 26.3 μg h^{-1} cm^{-2} and an FE of 15.4 %, far exceeding the activity of pristine Mo_2C. In addition, Liu *et al*. prepared ultrathin Ru nanosheets *via* a cyanide gel reduction method [63], generating a 3D-interconnected structure with high surface area, modulated electronic states, and low-coordination defects. The catalyst achieved 23.88 $\mu g\,h^{-1}\,cm^{-2}$, confirming the critical role of morphology and structure in NRR catalytic activity. In fact, Ru- and Rh-based catalysts are theoretically predicted to exhibit high intrinsic activity, occupying top positions in Skulason's volcano plot [64,65]. Numerous experimental studies have subsequently validated these predictions [66].

Overall, rational structural design and compositional tuning can substantially increase the specific surface area, optimize the distribution of active sites, and regulate the local chemical environment, thereby collectively enhancing NRR activity. However, for noble metal catalysts, the intrinsic activity toward the HER is typically higher than that toward NRR, causing a large fraction of the electrical energy to be consumed by hydrogen production and resulting in a low FE for ammonia synthesis. To address this challenge, strategies such as alloying with a second metal or anchoring noble metals onto suitable support have been widely employed to further enhance the NRR performance. The properties and key parameters of representative noble metal catalysts are summarized in Table 3.

5.2. Transition metal catalysts

Transition metal catalysts, characterized by their natural abundance, low cost, structural stability, and facile synthesis, have emerged as promising alternatives to noble metals for the NRR [67–69]. Notably, most biological N_2-fixation enzymes also rely on transition metals, inspiring the design and synthesis of a wide range of transition metal catalysts [70,71]. Current NRR transition metal systems primarily include Fe, Mo, Co, Ni, Cu, Zn, and their oxides, sulfides, nitrides, carbides, phosphides, and composites [72–75]. Among the various modification strategies, heteroatom doping and vacancy engineering are the two most common strategies to construct defects that significantly enhance the catalytic performance [76–78]. In this section, based on these two strategies, we summarize the synthesis methods, NRR performance, and catalytic mechanisms of representative transition metal catalysts [79–82].

Transition metal oxides are particularly compelling due to their high NRR activity, simple synthesis, and high stability, making them a popular choice for NRR [83–85]. Up to now, reported systems include oxides of Fe, Mn, Ti, Mo, and Cr. Among them, Fe_2O_3, a very common and cheap transition metal oxide, have been widely investigated for NRR [86,87]. Chen *et al*. developed electrochemically activated Fe_2O_3–CNT hybrids (Fig. 5a) [88], achieving an NH_3 yield of 41.6 $\mu g\,h^{-1}\,mg_{cat}^{-1}$ and an FE of 17 % in 0.1 mol/L KOH after 3-h activation. They confirmed a linear relationship between NH_3 production yield and the O^{2-} signal from γ-Fe_2O_3, highlighting the decisive role of oxygen vacancies in catalysis. Building on vacancy engineering, Wang *et al.* found that B-doped TiO_2 exhibits an increased number of oxygen vacancies [89], promoting semiconductor-to-metal transition that enhances electron transfer in the catalytic process. The optimized B-TiO_2–CPE catalyst achieved 14.4 μg h^{-1} mg_{cat}^{-1} and an FE of 2.5 % in 0.1 mol/L Na_2SO_4 (Fig. 5b), outperforming the undoped counterpart. Recognizing the interplay between electronic structure and vacancy formation, Xian *et al*. synthesized Fe-doped MoO_3 nanosheets featuring metallic electronic characteristics, expanded surface area, and abundant defects [90]. This catalyst achieved an NH_3 yield of 28.52 μg h^{-1} mg_{cat}^{-1} and an FE of 13.3 % at −0.70 V *vs.* RHE in 0.1 mol/L Na_2SO_4 (Figs. 5c and d). Vacancy creation and electronic structure modulation have also proven effective for suppressing HER. For example, Xie *et al.* designed a Mo/VO_2 catalyst *via* hydrothermal synthesis, where VO_2 serves both as a support and as an N_2 adsorption site [91]. Tailoring electronic interactions between Mo and VO_2 generated electron-deficient Mo Lewis acid sites that simultaneously suppress HER and facilitate N_2 activation (Fig. 5e). This configuration raises the energy barrier for HER and the first hydrogenation step, enhancing NRR selectivity by impeding H^+ adsorption at the active sites. Furthermore, V atoms facilitate N_2 activation by donating electrons

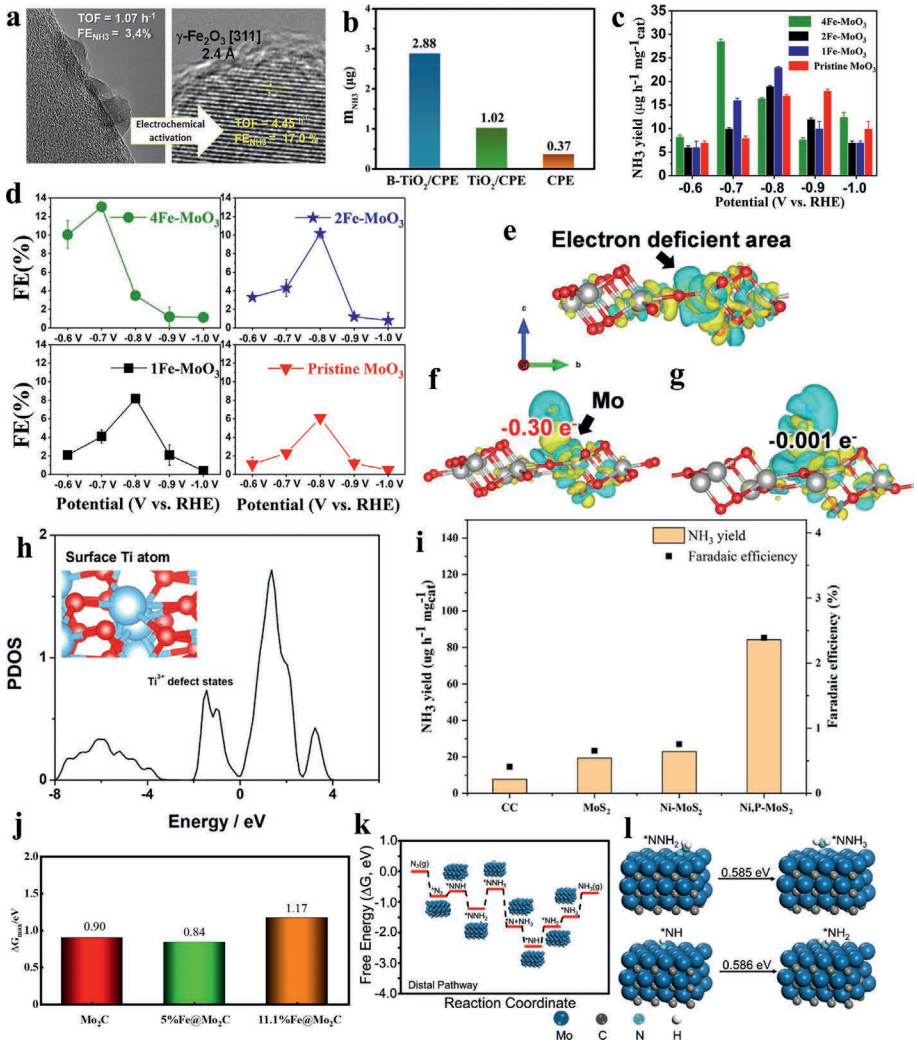


Fig. 5. (a) TEM images of *in-situ* activation-γ-Fe_2O_3. Copied with permission [88]. Copyright 2020, Elsevier. (b) NH_3 yield rate of different catalysts (B-TiO_2/CPE, TiO_2/CPE, CPE). Reproduced with permission [89]. Copyright 2019, American Chemical Society. (c, d) NH_3 yield and FE of electrocatalysis over 1, 2, 4 Fe-MoO_3 and pristine MoO_3 at various potentials. Reproduced with permission [90]. Copyright 2021, American Chemical Society. (e-g) Density functional theory calculation for NRR. Spheres: red = O, gray = V, cyan = Mo. (e) Charge density difference of Mo/VO_2. (f) Charge density difference of Mo/VO_2. (g) VO_2 for N_2 adsorption. Reproduced with permission [91]. Copyright 2023, Wiley-VCH GmbH. (h) PDOS of Ti^{3+} in Ti_2O_3 (012) surfaces (inset atom structure represents Ti^{3+} coordination structure). Reproduced with permission [92]. Copyright 2021, American Chemical Society. (i) NH_3 yield and FE of different electrodes at a potential of −0.50 V *vs.* RHE. Reproduced with permission [95]. Copyright 2024, Elsevier. (j) Reaction rate-determining step free energy diagram of Mo_2C with different Fe doping amounts. Reproduced with permission [99]. Copyright 2022, Elsevier. (k, l) Calculated free energy profile and the corresponding optimized structure for the NRR process on the α-Mo_2C (200) surface plane. Reproduced with permission [100]. Copyright 2020, American Chemical Society.

into its antibonding orbital (Figs. 5f and g). As a result, the catalyst delivered outstanding performance, achieving an NH_3 yield of 190.1 μg h^{-1} $mg_{cat}{}^{-1}$ and an FE of 32.4 % at −0.50 V *vs.* RHE in 0.05 mol/L H_2SO_4. Finally, Chen *et al.* introduced Ti^{3+} defects into TiO_2 (Fig. 5h) [92], creating five-coordinated metallic active centers confirmed by projected density of states (PDOS) analysis. These defects facilitate N_2 activation through bandgap defect states and orbital splitting, achieving an NH_3 yield of 26.01 μg h^{-1} $mg_{cat}{}^{-1}$ and an FE of 9.16 % at −0.25 V *vs.* RHE in 0.1 mol/L HCl.

Beyond oxides, transition metal sulfides have also been extensively explored as electrocatalysts for NRR under ambient conditions [93,94]. Among them, MoS_2 is a representative catalyst as its positively charged Mo edges can effectively adsorb and activate N_2 molecules, highlighting its strong catalytic potential. Enhancing the NRR performance of MoS_2 relies heavily on precisely regulating its electronic structure and the coordination microenvironment of its active sites. This principle is well exemplified by doping strategies. For instance, Duan *et al.* synthesized two-dimensional Ni-P co-doped MoS_2 catalysts *via* hydrothermal methods [95]. Compared with undoped and singly-doped counterparts, the Ni-P@MoS_2 exhibited markedly improved NRR activity, achieving an NH_3 yield of 84.29 μg h^{-1} $mg_{cat}{}^{-1}$ and an FE of 2.39 % at −0.50 V *vs.* RHE (Fig. 5i). Ni doping induces a semiconductor-to-metallic phase transition, while P incorporation generates sulfur vacancies that act as N_2 adsorption sites.

Beyond elemental doping, ingenious nanostructure design offers another pathway to tailor active sites. Researchers developed monolayer MoS_2 with adjacent Mo sites (A-Mo-MoS_2) to simultaneously optimize N_2 activation and suppress HER [96]. The coordination unsaturated Mo sites create spin-delocalized electron fields through unpaired spin-polarized electrons along Mo edges. Gibbs free energy calculations indicated that these spin-delocalized electrons promote N_2 adsorption and activation, shifting the rate-determining step from energy-intensive $^*N_2$ hydrogenation to the

Table 4
Types and properties of representative transition metal catalysts.[a]

Electrocatalyst	Electrolyte	Potential (V *vs.* RHE)	Yield rate of NH_3 ($\mu g\ h^{-1}\ mg_{cat}^{-1}$)	FE (%)	Ref.
Fe_2O_3-CNT	0.1 mol/L KOH	−0.50	41.60	17.0	[88]
B-TiO_2-CPE	0.1 mol/L Na_2SO_4	−0.80	14.40	2.5	[89]
Fe@MoO_3	0.1 mol/L Na_2SO_4	−0.70	28.52	13.3	[90]
Mo/VO_2	0.05 mol/L H_2SO_4	−0.50	190.10	32.4	[91]
Ti_2O_3	0.1 mol/L HCl	−0.25	26.01	9.2	[92]
Ni-P@MoS_2	0.005 mol/L H_2SO_4	−0.50	84.29	2.4	[95]
A-MO-MoS_2	0.5 mol/L H_2SO_4	−0.20	48.80	27.3	[96]
Fe@MoS_2	0.5 mol/L K_2SO_4	−0.30	8.63	18.8	[97]
Fe@Mo_2C	0.1 mol/L Na_2SO_4	−0.30	36.60	10.3	[99]
α-Mo_2C	0.1 mol/L Na_2SO_4	−0.55	3.36 [b]	40.2	[100]

[a] Testing condition: room temperature/atmospheric pressure; N_2 flow rate (about 20 mL/min).
[b] The unit is $\mu g\ h^{-1}\ cm^{-2}$.

more favorable *HNNH hydrogenation. As a result, this catalyst achieved an NH_3 yield of 48.8 μg h^{-1} mg_{cat}^{-1} and an FE of 27.3% at −0.20 V *vs.* RHE in 0.5 mol/L H_2SO_4.

In addition, introducing other metal centers to create synergistic effects presents a powerful strategy. Inspired by the synergistic effects between Fe and Mo centers in natural nitrogenase, Su *et al.* decorated MoS_2 with Fe single atoms *via* hydrothermal synthesis [97]. The introduction of Fe single atoms significantly lowered the energy barrier for nitrogen fixation and suppressed the HER, enabling an NH_3 yield of 8.63 μg h^{-1} mg_{cat}^{-1} and an FE of 18.8% at −0.30 V *vs.* RHE in 0.5 mol/L K_2SO_4.

Transition metal carbides, which contain unoccupied d orbitals, also display strong N_2 adsorption capability. Because the sp-hybridized states of the transition metal in carbides migrate to the surface and hybridize with metal d-orbital and carbon s states, the excess occupied orbitals provide enhanced back-donation to the π orbitals of the absorbates [98]. This theoretical advantage has been strongly validated experimentally. For instance, Tao *et al.* investigated Fe-doped Mo_2C, confirming that 5% Fe incorporation maintains structural integrity while substantially modulating the electronic structure [99]. As shown in Fig. 5j, this modification enhanced N_2 activation, leading to an NH_3 yield of 36.60 μg h^{-1} mg_{cat}^{-1} and an FE of 10.3%. at −0.30 V *vs.* RHE in 0.1 mol/L Na_2SO_4.

The potential of metal carbides extends beyond doping. To further demonstrate their inherent ability to suppress HER, Ba *et al.* synthesized single-faceted α-Mo_2C (200) films *via* CVD [100]. This catalyst effectively suppressed HER and delivered an exceptional FE of 40.2% under ambient conditions, surpassing many conventional transition-metal systems. DFT calculations revealed that the $^*NNH_2 \rightarrow {}^*NNH_3$ and $^*NH \rightarrow {}^*NH_2$ steps serve as the rate-determining transitions (Figs. 5k and l), proceeding *via* a proton-coupled electron transfer along an associative distal pathway, which lowers NRR energy barriers.

Beyond these examples, other transition metal compounds such as Mo_2N nanorods [101,102] and Mo_2C nanometers have also demonstrated remarkable capabilities in suppressing HER and promoting N_2 adsorption [103].

Overall, the performance improvement of transition metal-based electrocatalysts primarily relies on defect engineering and electronic structure modulation (*e.g.*, oxygen/sulfur vacancies and heteroatom doping) to promote N_2 activation and suppress HER. However, the low active site density, imbalanced adsorption of intermediates, and insufficient stability often lead to reduced FE and activity degradation. To overcome these limitations, advanced strategies, including heteroatom doping (B, P, S, and O), construction of Lewis acid sites, and integration with suitable supports such as carbon nitride, have been widely adopted to modulate their electronic structure, thereby optimizing catalytic performance. The properties and parameters of representative transition metal catalysts are summarized in Table 4.

5.3. Single-atom catalysts

Single-atom catalysts (SACs) consist of isolated single metal atoms anchored on solid substrates (supports) to form atomic-level active sites [104]. Compared with conventional metal catalysts, SACs maximize atomic utilization efficiency and significantly reduce metal consumption [105]. The atomic-level active centers exhibit distinctive electronic properties characterized by high surface free energy, unsaturated coordination environments, and quantum size effects [106]. These attributes make SACs highly attractive for electrocatalytic NRR. When the interaction between metal atoms and supports is precisely regulated, SACs can achieve exceptional stability and catalytic activity [107]. Dual-atom catalysts (DACs) and single-atom alloys (SAAs) follow similar principles, providing additional design flexibility. Notably, the choice of support material critically influences NRR performance [108,109]. At present, common supports include nitride, graphene [98], black phosphorous (BP) [109], nitrogen-doped carbon [108], and MXene materials [110]. In this section, we summary some representative SACs and compare their key properties and performance metrics in Table 5.

The concept of SACs was pioneered by Zhang's group in 2011 with the synthesis of FeO_x-supported SACs, marking the beginning of rapid advancements in this field [111]. Several representative SACs systems are highlighted below. Zang *et al.* constructed a Cu single-atom catalyst (NC–Cu SA) supported on N-doped carbon (Fig. 6a) [112]. The isolated Cu atoms serve as active sites, while N coordination modulates their electronic structure, enhancing N_2 activation. The electrocatalyst achieved high NH_3 yields of 53.3 and 49.3 μg h^{-1} mg_{cat}^{-1} with FEs of 13.8% and 11.7% at −0.30 V *vs.* RHE in 0.1 mol/L KOH and 0.1 mol/L HCl, respectively, and showed excellent stability. Beyond Cu-based SACs, Co-, Ru-, and Rh-based SACs have also shown promising activity. For example, Zhang *et al.* doped Co into $LaNiO_3$ (Co-LNO) to produce a series of Co-LNO materials [107]. Among them, Co-LNO-3 showed optimal electrocatalytic reduction performance, achieving an NH_3 yield of 14.57 μg h^{-1} mg_{cat}^{-1} and an FE of 26.44% at −0.10 V *vs.* RHE in 0.01 mol/L K_2SO_4. Theoretical simulations revealed that the synergy between Co dopants and oxygen vacancies optimizes the electronic structure and reduces reaction energy barriers. In another system, Tao *et al.* loaded isolated Ru atoms onto N-doped porous carbon anchored on ZrO_2 nanoparticles *via* pyrolysis [113], achieving a maximum NH_3 yield of 3.67 μg h^{-1} mg_{cat}^{-1} at −0.21 V *vs.* RHE. Yang *et al.* also developed a Ru-S-C single-atom catalyst based on Ru single atoms and verified its Ru/S dual-site synergistic catalytic mechanism [114]. In this system, the Ru site is responsible for adsorbing N_2, while the adjacent S site adsorbs H^+, creating an "electron push-push" effect that promotes N_2 activation and its first protonation step, thereby substantially lowering the reaction energy barrier (Fig. 6b). As a result, the catalyst exhibits excellent NRR performance, achieving an NH_3 yield of 13.18 μg h^{-1} mg_{cat}^{-1}.

Table 5
Types and properties of representative single atom catalysts.[a]

Electrocatalyst	Electrolyte	Potential (V *vs.* RHE)	Yield rate of NH_3 ($\mu g\ h^{-1}\ mg_{cat}^{-1}$)	FE (%)	Ref.
Co-LNO-3	0.01 mol/L K_2SO_4	−0.10	14.57	26.4	[107]
NC–Cu SA	0.1 mol/L KOH/HCl	−0.30	53.30/49.30	13.8/11.7	[112]
Ru@ZrO_2	0.1 mol/L HCl	−0.21/−0.11	3.67	21.0	[113]
Ru-S-C	0.1 mol/L KOH	−0.15	13.18	6.0	[114]
Rh_1/MnO_2	WISE	−0.50	271.80	73.3	[115]
NC@NiCu	0.1 mol/L Na_2SO_4	−0.20	70.78	30.0	[120]
DA-MnCu/NC	0.5 mol/L $NaBF_4$	−0.15	88.34	67.8	[121]
RuNi	0.1 mol/L Na_2SO_4	−0.20/−0.10	5.07 [b]	26.2	[122]
$PdFe_1$	0.5 mol/L $LiClO_4$	−0.20	111.90	37.8	[123]
Ru-Cu-CPs	0.1 mol/L HCl	−0.10	73.00 [c]	31.0	[124]

[a] Testing condition: room temperature/atmospheric pressure; N_2 flow rate (about 20 mL/min).
[b] The unit is $\mu g\ h^{-1}\ cm^{-2}$.
[c] The unit is $\mu mol\ h^{-1}\ mg_{cat}^{-1}$.

Shen *et al*. developed a Rh_1/MnO_2 SAC by anchoring single-atom Rh on MnO_2 (Fig. 6c) [115], achieving a record-breaking NH_3 yield of 271.80 $\mu g\ h^{-1}\ mg_{cat}^{-1}$ and an FE of 73.3 % in a K_2SO_4 brine electrolyte (WISE). The WISE strategy effectively suppressed HER, promoted N_2 enrichment on the catalyst surface, and facilitated N_2 activation and hydrogenation at the Rh active sites. These findings highlight the profound influence of electrolyte properties (pH, concentration, ionic composition, temperature) on NRR performance [116].

DACs provide another strategy to improve NRR activity. By introducing direct metal-metal electronic coupling, DACs generate novel electronic structures with optimized adsorption energies for reaction intermediates [117–119]. This coupling represents the fundamental distinction from SACs. Yang *et al*. prepared a Ni-Cu DAC on N-doped porous carbon (NC@NiCu) by electrochemical deposition [120]. NC@NiCu achieved an NH_3 yield of 70.78 $\mu g\ h^{-1}\ mg_{cat}^{-1}$ and an FE of 30.0 %, outperforming monometallic SACs. DFT calculations showed the $^*N_2H \rightarrow NHNH$ step has a higher energy barrier (0.72 eV) than the $^*N_2H \rightarrow {}^*NNH_2$ step (0.69 eV), indicating preferential distal pathway kinetics (Fig. 6d). The superior performance stems from synergistic intermetallic electron transfer that modulates reaction energy barriers and stabilizes key intermediates. Using a similar approach, Biswas *et al.* successfully constructed Mn-Cu bonded diatomic sites on a nitrogen-doped carbon substrate [121]. In this system, Mn exhibits an electron-deficient state due to electron transfer to Cu, while Cu becomes electron-rich, resulting in a localized asymmetric electronic distribution. This charge redistribution effectively enhances N_2 adsorption on Mn sites and facilitates the activation of the N≡N bond. Ultimately, at −0.15 V *vs*. RHE, the catalyst delivers an NH_3 yield of 88.34 $\mu g\ h^{-1}\ mg_{cat}^{-1}$ and an FE of 67.76 %, representing a fourfold improvement compared with the corresponding single-atom Mn catalyst. Additionally, Zhang *et al*. proposed a RuNi dual-site catalyst [122], in which Ru sites are responsible for N_2 adsorption and activation, while Ni sites supply H^+. This synergistic mechanism optimizes the adsorption strength of the NRR intermediate $^*N_2H$ and facilitates NH_3 desorption, enabling active site regeneration. In 0.1 mol/L Na_2SO_4, the catalyst achieves an NH_3 yield of 5.07 $\mu g\ h^{-1}\ cm^{-2}$ at −0.2 V *vs*. RHE with an FE of 26.2 % at −0.1 V *vs*. RHE, surpassing the performance of most reported Ru-based catalysts.

Different from SACs, SAAs combines the atomic efficiency of SACs with the stability of alloys, effectively preventing metal aggregation while maximizing active site exposure. Li *et al.* demonstrated this potential by engineering a $PdFe_1$ SAA *via* wet-chemical fixation of Fe atoms on Pd carriers [123]. Charge density analysis showed that Fe atoms become electron-deficient when coordinated with Pd (Fig. 6e), creating Lewis acid sites capable of accepting electron donation from N_2 (Fig. 6f). Compared with pure Pd, the $PdFe_1$ SAA exhibited substantially stronger N_2 activation, yielding 111.90 $\mu g\ h^{-1}\ mg_{cat}^{-1}$ NH_3 with a FE of 37.8 % at −0.20 V *vs*. RHE and maintaining stability for more than 100 h (Figs. 6g and h). Extending the SAA concept to immiscible metals, Kim *et al*. employed carbon thermal shock (CTS) to synthesize a series of Ru-based SAAs (Ru-Cu, Ru-Rh, Ru-Pt, Ru-Co) with atomic-scale dispersion on carbon nanotubes [124]. Among these, Ru-Cu-CPs exhibited superior NRR performance, with an FE of 31 % and an NH_3 yield of 73 $\mu mol\ h^{-1}\ mg_{cat}^{-1}$. The results showed that Ru sites facilitate N_2 adsorption and activation, where Cu modulates the electronic structure, thus optimizing intermediate adsorption and lowering the energy barrier. DFT calculations identified the distal pathway as the most favorable, with RuCu (101) exhibiting stronger N_2 activation than pure Ru (101), as evidenced by more negative ΔG values for $^*NNH$ formation (0.75 *vs*. 0.92 eV) and N_2 adsorption (−0.26 *vs*. −0.02 eV) (Figs. 5i–l).

SACs, despite being highly promising catalytic materials, still face challenges in practical applications such as insufficient stability and susceptibility to deactivation. Moreover, traditional synthesis methods mostly rely on high-temperature pyrolysis-based "top-down" strategies, often suffering from poor controllability over atomic structures and structural heterogeneity of active sites. Accordingly, future development should focus on milder and more precise "bottom-up" synthetic routes. For example, solution-phase self-assembly or low-temperature template-assisted methods offer viable pathways for the controlled preparation of precursors with well-defined molecular structures and clear metal-coordination environments.

5.4. Metal-organic frameworks catalysts

Metal-organic frameworks (MOFs), featuring ordered pore structures, high specific surface area, and tunable chemical functionalities, are ideal platforms for achieving high-density dispersion of active sites [125,126]. In electrocatalytic NRR, MOFs offer abundant catalytic active centers with strong metal sites that facilitate N_2 adsorption and activation [127,128].

In 2017, Zhao *et al*. first employed the use of three unmodified MOFs materials [MOF(Fe), MOF(Co), and MOF(Cu) (MIL-100(Fe), ZIF-67, and HKUST-1)] as electrocatalysts for NRR [129]. These materials possess distinct metal centers and high specific surface areas, enabling efficient N_2 adsorption. The uniformly distributed metal ions (Fe^{3+}, Co^{2+}, and Cu^{2+}) with empty d-orbitals serve as Lewis acid sites, which weaken the N≡N triple bond by extracting electrons from N_2 molecules, thereby promoting NH_3 generation. Among them, MOF(Fe) exhibited the optimal NH_3 production rate of 1.52×10^{-9} mol s^{-1} cm^{-2} with an FE of 0.88 % (Figs. 7a and b). Although the FE was low, this pioneering study established the foundation for developing MOF-derived NRR catalysts.

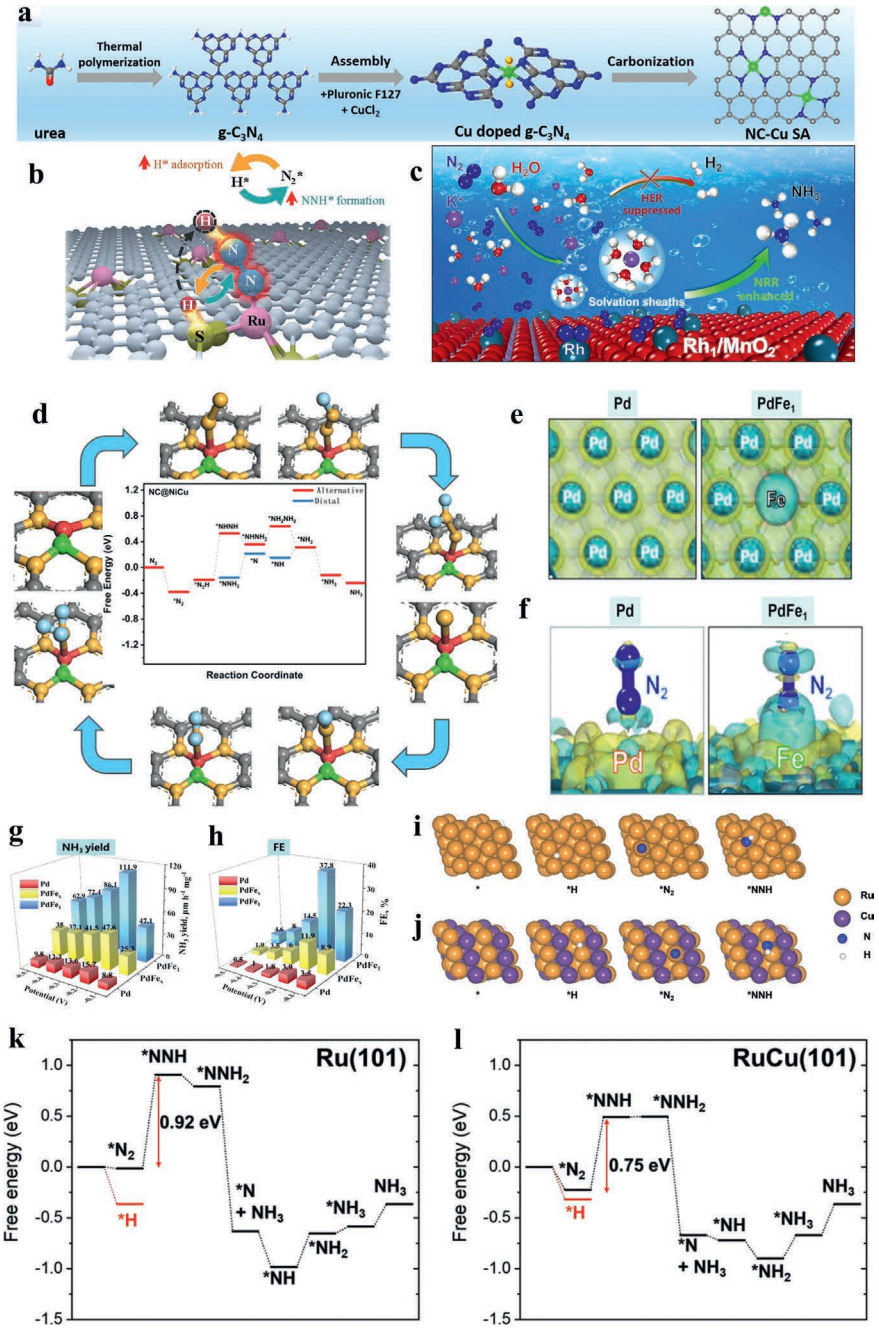


Fig. 6. (a) Schematic illustration of NC–Cu SA electrocatalytic reduction of N_2 to NH_3. Reproduced with permission [112]. Copyright 2019, American Chemical Society. (b) Schematic diagram of the Ru/S dual-site collaborative catalytic mechanism. Reproduced with permission [114]. Copyright 2022, Elsevier. (c) Schematic diagram of rhodium single-atom catalyst (Rh_1/MnO_2) in salt electrolyte. Copied with permission [115]. Copyright 2022, Elsevier. (d) Free energy diagram of the NRR with a distal and alternative pathway on NC@NiCu. Reproduced with permission [120]. Copyright 2025, American Chemical Society. (e) Differential charge density of Pd and $PdFe_1$. (f) The differential charge density of N_2 adsorbed on Pd and $PdFe_1$. (g) FE of Pd, $PdFe_x$ and $PdFe_1$ at different potential. (h) NH_3 yields at various applied potentials of Pd, $PdFe_x$ and $PdFe_1$. Reproduced with permission [123]. Copyright 2022, Wiley-VCH GmbH. (i, j) Optimized geometries of *, *H, $*N_2$, and *NNH on (i) Ru (101) and (j) Ru-Cu (101). (k, l) Corresponding free-energy diagrams for the NRR pathway and the competing hydrogen adsorption process on (k) Ru (101) and (l) Ru-Cu (101). Color code: Ru (gray), Cu (green), N (blue), H (white). Reproduced with permission [124]. Copyright 2022, Wiley-VCH GmbH.

Subsequently, most studies have focused on the designing and modifying MOF materials to improve their NRR activity [130,131]. Defect engineering and interface engineering are two major strategies for enhancing NRR performance [132,133]. As a typical defect engineering approach, creating vacancies can generate localized electron-rich sites that significantly improve NRR yield. For instance, Wen *et al.* successfully prepared oxygen vacancy-rich Zn-doped Co_3O_4 nanopolyhedra and demonstrated that Zn-doped Zn-Co_3O_4 achieved optimal NH_3 yield and FE (Fig. 7c) [134]. Zn doping not only introduced abundant oxygen vacancies as active sites for N_2 adsorption but also modulated the electronic structure of Co sites, thereby optimizing the adsorption energy of N_2 and reaction intermediates (Fig. 7d). This synergistic strategy combining oxygen vacancy creation and metal doping provides an effective approach for designing highly efficient and stable NRR electrocatalysts.

In interface engineering, modulating the distribution of oxygen vacancies and interfacial electronic interactions can further optimize catalytic pathways [135]. For example, Luo *et al.* developed a

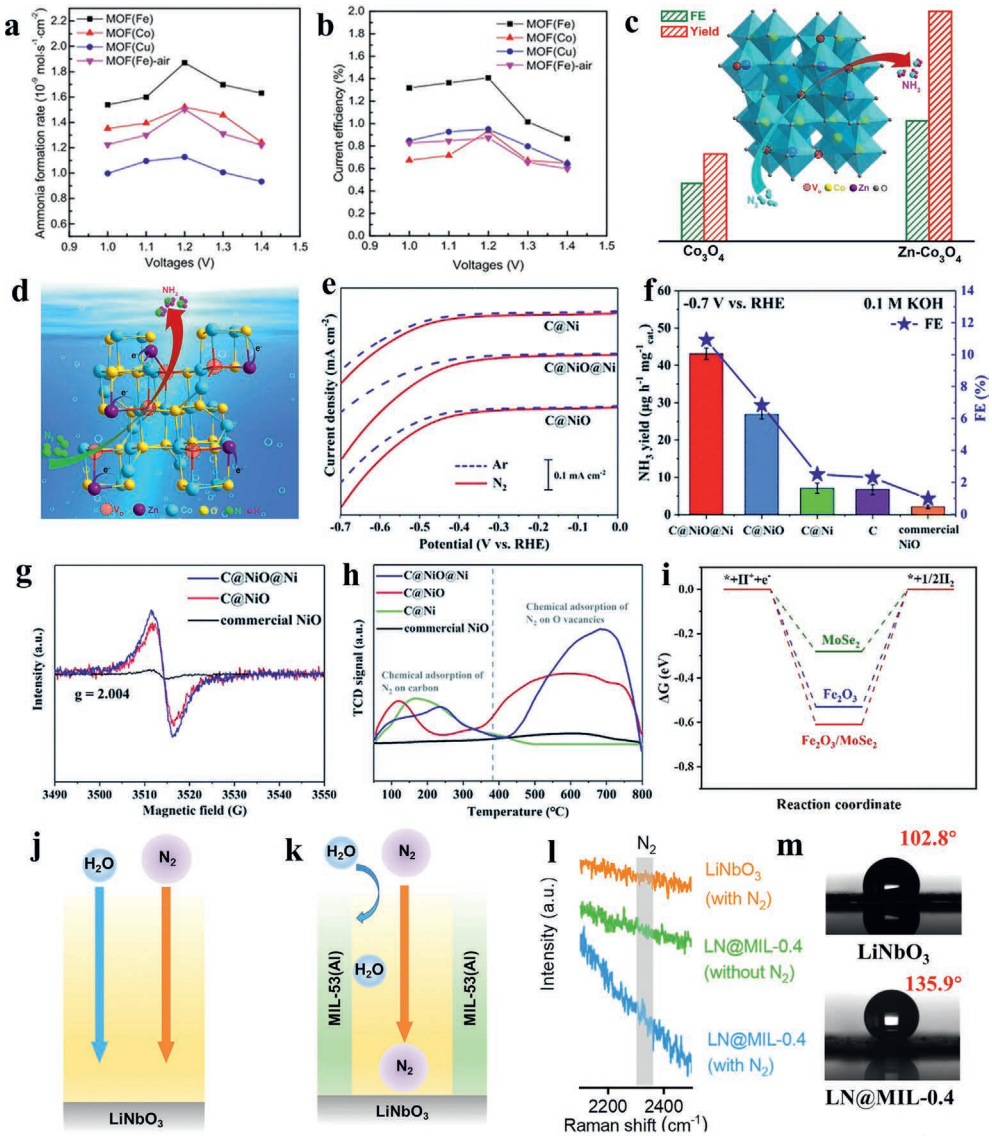


Fig. 7. (a) Comparative electrochemical properties of MOF(Fe), MOF(Co), MOF(Cu). (b) Current efficiency on series MOFs. Reproduced with permission [129]. Copyright 2017, Springer Science Business Media New York. (c) Performance comparison diagram of Co_3O_4 and Zn-Co_3O_4. (d) Schematic diagram of the electrochemical NRR based on Zn-Co_3O_4. Reproduced with permission [134]. Copyright 2021, American Chemical Society. (e) LSV curves of C@Ni, C@NiO@Ni and C@NiO in Ar or N_2-saturated 0.1 mol/L KOH. (f) The NRR performance of different catalysts at −0.70 V. (g) EPR spectra of C@NiO@Ni, C@NiO and commercial NiO. (h) The N_2-TPD profiles of C@NiO@Ni, C@NiO, C@Ni and commercial NiO. Reproduced with permission [136]. Copyright 2020, Royal Society of Chemistry. (i) Adsorption energy comparison of the catalytic activity for the HER. Reproduced with permission [137]. Copyright 2023, Royal Society of Chemistry. (j) Schematic depicting of $LiNbO_3$ during the NRR process. (k) Schematic depicting of $LiNbO_3$@MIL-53(Al) during the NRR process. (l) Qualitative comparisons of Raman spectra of the different smaples obtained under various experimental conditions. (m) Water contact angle images of $LiNbO_3$ and LN@MIL-0.4. Reproduced with permission [138]. Copyright 2025, Elsevier.

hollow C@NiO@Ni catalyst with uniformly distributed Ni/NiO heterointerfaces [136]. The catalyst achieved excellent performance (Figs. 7e and f), with an NH_3 yield of 43.15 μg h^{-1} mg_{cat}^{-1} and an FE of 10.9% at −0.70 V *vs.* RHE. The exceptional NRR activity is attributed to a high concentration of oxygen vacancies in NiO and abundant NiO/Ni interfaces. Specifically, the oxygen vacancies function as nitrogen activation sites, whereas the NiO/Ni interface addresses the critical challenge of proton capture in alkaline electrolytes (Figs. 7g and h). Using a similar interface engineering strategy, Huang *et al.* constructed a Fe_2O_3/$MoSe_2$ electrocatalyst comprising MOF-derived Fe_2O_3 nanoparticles combined with $MoSe_2$ nanoflowers [137]. The catalyst achieved an NH_3 yield of 46.25 μg h^{-1} mg_{cat}^{-1} and an FE of 9.6% in 0.05 mol/L H_2SO_4 electrolyte, along with excellent cycling stability. They confirmed that strong electron transfer between Fe_2O_3 and $MoSe_2$ can form an internal electric field that enhanced interfacial charge transfer capacity and promoted N_2 adsorption and activation. Additionally, Se vacancies introduced additional Mo active sites while suppressing the HER, thereby improving NRR selectivity (Fig. 7i).

Furthermore, MOFs can leverage their inherent hydrophobicity and porosity to serve as interfacial supports or modifiers for modulating the catalytic performance of other electrocatalysts. For instance, Zhang *et al.* developed a $LiNbO_3$@MIL-53(AI) composite electrocatalyst, demonstrating the effectiveness of MOF membrane-based interface engineering in enhancing NRR performance [138]. The MIL-53(AI) membrane plays a dual role: it enriches N_2 at the catalyst interface while increasing surface hydrophobicity to suppress the competing HER (Figs. 7j and k). *In-situ* Raman spectroscopy demonstrated enhanced N_2 adsorption capability in LN@MIL-0.4 (Fig. 7l). Contact angle measurements further verified that the increased hydrophobicity reduces water coverage on active sites and suppress HER (Fig. 7m). As a result, the opti-

mized catalyst achieved an NH_3 yield of 45.25 μg h^{-1} $mg_{cat}{}^{-1}$ and an FE of 86.41 % at −0.45 V *vs.* RHE in 0.1 mol/L Na_2SO_4.

In recent years, theoretical calculations have emerged as a crucial tool for predicting and guiding the application of MOFs in nitrogen fixation. Xiong *et al.* performed first-principles calculations to systematically screen $TM_3(HITP)_2$ materials through a three-step strategy, identifying $Mo_3(HITP)_2$ and $Os_3(HITP)_2$ as efficient NRR catalysts with limiting potentials of −0.39 and −0.43 V, respectively [139]. Electronic structure analysis revealed that the activity stems from a σ-donation-π^*-backdonation mechanism, where the closer energy alignment between unoccupied Mo 4d orbitals and the N_2 antibonding orbitals enables superior performance. Notably, both catalysts also exhibit high HER limiting potentials, ensuring excellent NRR selectivity. Similarly, Almheir *et al*. employed DFT to investigate the NRR performance of two-dimensional TM-Tp MOFs using triformylbenzoic acid as the ligand [140]. Through structural modeling, a two-step screening process based on N_2 adsorption free energy and NNH intermediate stability, combined with reaction free energy diagram calculations, they identified the Mo-Tp system as a highly active NRR catalyst. Its distal reaction pathway shows a limiting potential of −0.38 V and a theoretical FE approaching 100 %. Furthermore, using electronic structure analysis methods such as density of states (DOS), crystal orbital Hamilton population (COHP), Bader charge analysis, and spin density, they revealed that the asymmetric coordination environment of the Mo active center effectively modulates its d-band characteristics and charge transfer mechanism. As purely computational studies, these works not only pinpoint promising MOF-based NRR catalysts but also establish a conceptual framework for transitioning NRR research from trial-and-error experimentation toward rational catalyst design.

In summary, MOFs and MOF-derived materials have emerged as promising electrocatalysts for NRR owing to their structural diversity, tunable porosity, and flexible defect/interface engineering capabilities [141]. However, inherent drawbacks such as poor electrochemical stability, low conductivity, insufficient active site density, and mass transfer limitations lead to low FE and activity degradation. Future progress will require precise design of active centers guided by theoretical calculations [142], the development of stable and conductive composite of MOF-derived materials, and their integration with gas diffusion electrodes and non-aqueous electrolyte systems to achieve substantial performance improvement.

5.5. Nonmetallic-based catalysts

Compared with metal-based catalysts, non-metal-based catalysts possess advantages such as abundant resources, low cost, environmental friendliness, and unique electronic structures [143]. Consequently, non-metal catalysts have attracted increasing attention in recent years [144]. Common non-metal-based catalysts include carbon-based materials (*i.e.*, graphene, graphene oxide, porous carbon), carbon nitride, boron-based materials, covalent organic frameworks (COFs), and others [145,146].

5.5.1. Carbon-based catalysts

Carbon materials were traditionally considered poor electrocatalysts for the NRR owing to their inherent chemical inertness, weak N_2 adsorption capability, strong competition from HER, and lack of intrinsic active sites [147]. Nevertheless, they are widely used as catalyst support matrices because of their ultrahigh surface area (up to 2600 m^2/g), excellent stability, and good electrical conductivity. To harness these advantages, extensive research has focused on transforming carbon materials into active NRR catalysts. Currently functional group tailoring and heteroatom doping are the two major strategies for constructing catalytic sites [148]. Below, we summarize the construction methods, catalytic performance, and underlying mechanisms of reduced graphene, graphene oxide, and porous carbon-based catalysts [149,150].

Functional group engineering modulates the electronic structure of carbon substrates, redistributes charge, and generates active sites. Song *et al.* utilized oxygen-enriched tannic acid (TA) to functionalize reduced graphene oxide (rGO) [151]. TA was anchored onto the graphene lattice *via* strong π-π stacking interactions and modulated the electronic structure of adjacent carbon atoms affected by its oxygen functional groups. Owing to the high electronegativity of oxygen atoms, charge in rGO was redistributed, producing active sites. The resulting catalyst exhibited stable performance, achieving an NH_3 yield of 17.02 μg h^{-1} $mg_{cat}{}^{-1}$ and an FE of 4.83 % at the optimized potential. Using a similar approach, Song *et al.* developed oxygen-functionalized 3D porous carbon to suppress HER [152]. The modified catalyst delivered an FE of 16.5 % and an NH_3 yield of 32.20 μg h^{-1} $mg_{cat}{}^{-1}$, which was 3.3 times higher than unmodified carbon in 0.05 mol/L H_2SO_4 (Figs. 8a and b). Stability was maintained for up to 12 h (Fig. 8c). DFT calculations revealed that oxygen functional groups lower the reaction energy barrier, suppress HER, and promote N_2 electroreduction.

Heteroatom doping introduces catalytically active sites and facilitates electron transfer pathways. Depending on dopant type, doping can be categorized as metal and non-metal doping. For metal doping systems, Yan *et al.* anchored 12 transition metals (*e.g.*, Fe, Mo, Ru) onto defective graphene containing carbon vacancies (Fig. 8d) [153]. They found that tuning the metal center and its coordination environments (C_3, N_3, C_4, N_4) significantly modulates the electronic structure and catalytic performance. Subsequently, Wang *et al.* leveraged large-scale constant-potential simulations to evaluate SACs (M_1/N-graphene, M = Mo, W, Fe, *etc.*), overcoming the limitations of charge-neutral methods [154]. They identified W_1/N-graphene as a promising catalyst with a remarkably low limiting potential of −0.13 V *vs.* RHE, attributed to potential-dependent charge modulation and Fermi level tuning (Figs. 8e and f). The study further designed Fe-N_4–C configurations and clarified rate-determining steps (*NNH, *NH_2), showing how defect engineering enhances graphene-based NRR performance.

For non-metal doping, Yu *et al.* reported B-doped graphene (BG-1) catalyst achieving an NH_3 yield 9.8 μg h^{-1} $mg_{cat}{}^{-1}$ and an FE of 10.8 % at −0.50 V *vs.* RHE in 0.05 mol/L H_2SO_4 [155]. Compared with undoped graphene, B-doped graphene exhibited asymmetric electron density (Fig. 8g). They attributed the enhanced activity to electron redistribution induced by B, which acts as a Lewis acid and accelerates N_2 desorption (Fig. 8h). Similarly, Wu *et al.* reported a phosphorus-doped graphene and revealed that PG/CP was the most active among CP, G/CP, and PG/CP electrodes (Fig. 8i) [156]. It achieved an NH_3 yield of 32.33 μg h^{-1} $mg_{cat}{}^{-1}$ with an FE of 20.82 % at −0.50 V *vs.* RHE in 0.5 mol/L $LiClO_4$ (Fig. 8j). The electron-donating nature of P enhanced charge transfer and reduced the energy barrier for NH_3 formation.

Co-doping with metal and non-metal species has also proven highly effective for enhancing NRR properties. For instance, Zhao *et al.* successfully synthesized Fe-immobilized B/N co-doped carbon materials (Fe-B/N–C) through a sequential solvothermal and high-temperature calcination approach [157]. The optimized catalyst demonstrated exceptional electrocatalytic performance, achieving an impressive NH_3 yield of 100.1 μg h^{-1} $mg_{cat}{}^{-1}$ with an FE of 23.0 % at −0.40 V *vs.* RHE. Structural analysis confirmed the formation of N-B coordination within Fe-N_4 sites, which effectively modulated the Fe electronic structure, increasing its positive charge (0.99 e for Fe-N_4-B *vs.* 0.88 e for Fe-N_4) (Fig. 8k). This electronic tuning enhanced activation of key intermediates and facilitated N_2 adsorption and activation through Lewis acid-base interactions (Fig. 8l).

In summary, functional group engineering and heteroatom doping (including both metal and non-metal doping) provide effec-

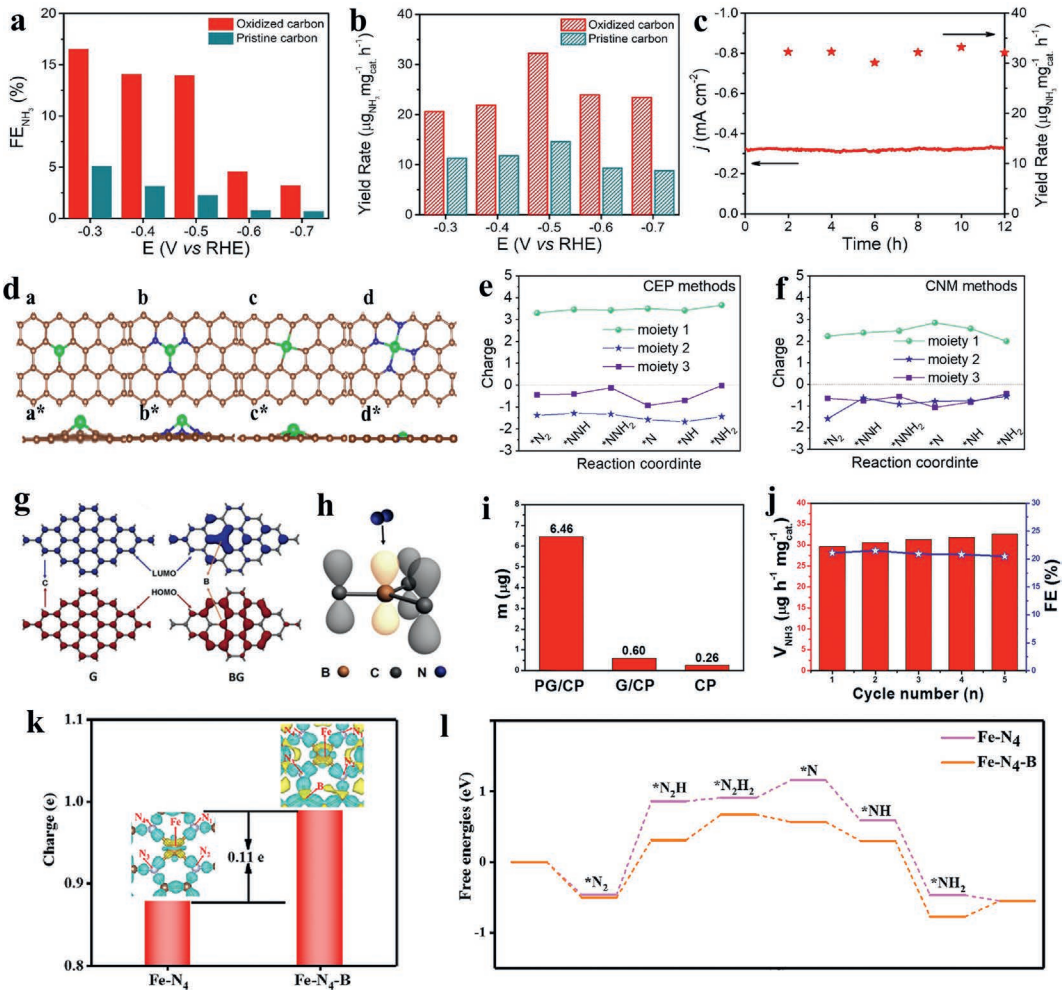


Fig. 8. (a, b) FE and NH_3 yield rate of oxidized carbon and pristine carbon at different applied potentials. (c) 12 h durability test of oxidized carbon at −0.50 V *vs.* RHE in N_2-saturated 0.05 mol/L H_2SO_4 electrolyte. Reproduced with permission [152]. Copyright 2022, Elsevier. (d) Optimized configurations of 12 single-atom catalysts supported on defective graphene substrates: (up) top views and (down) side views. Brown for C, blue for N, and green for Fe, Mo, or Ru. Reproduced with permission [153]. Copyright 2021, American Chemical Society. (e) Constant-potential DFT and (f) CNM calculations of the charge variation for key moieties on W_1/N-graphene along the reaction pathway. The monitored moieties are: graphene (1), the W_1-N_3 active center (2), and the adsorbed NxHy species (3). Reproduced with permission [154]. Copyright 2025, Elsevier. (g) LUMO (blue) and HOMO (red) of undoped G (left) and BG (right). The position of a single doped boron atom was labeled. (h) Schematic of the atomic orbital of BC_3 for binding N_2. Reproduced with permission [155]. Copyright 2018, Elsevier. (i) Amounts of NH_3 with different electrodes. (j) NH_3 yields and FEs for PG/CP at −0.65 V. Reproduced with permission [156]. Copyright 2020, Royal Society of Chemistry. (k) Charges of Fe atoms in the different structures. (l) Gibbs free energy calculated for the different structures and schematic diagram of the changes in the NRR process. Reproduced with permission [157]. Copyright 2023, Elsevier.

tive strategies for modifying carbon-based materials, enabling electronic structure regulation, active-site creation, and suppression of the competing HER.

5.5.2. Carbon-nitrogen catalysts

Compared with traditional carbonaceous materials, carbon nitride features a distinctive structure in which the incorporation of nitrogen atoms not only disrupts surface inertness but also fundamentally modifies the electronic configuration. This architecture offers electron-rich nitrogen sites capable of efficiently adsorbing and activating reactant molecules, thereby offering remarkable catalytic advantages. Among various carbon nitride materials, graphitic carbon nitride (g-C_3N_4) is the most extensively studied and widely applied owing to its thin and porous framework that is easily modified and doped. Currently, introducing metal or nonmetal heteroatoms to construct surface defects in g-C_3N_4 represents a dominant strategy for enhancing NRR performance.

Numerous studies have demonstrated that metal-doped g-C_3N_4 is an efficient strategy to achieving high NH_3 yield [158–160]. A representative example is the Zr-doped g-C_3N_4 reported by Lin *et al.* [161]. They successfully regulated the electronic structure of g-C_3N_4 by the introduction of Zr element and confirmed that a large number of C vacancies and defect sites in the Zr-C_3N_4 skeleton generated during the doping process (Fig. 9a). The introduction of Zr also led to a sponge-like mesoporous morphology with a regular layered structure, resulting in an NH_3 yield of 5.28 μg h^{-1} mg_{cat}^{-1} and an FE of 11.54% at −0.10 V *vs.* RHE. Chu *et al.* further constructed a 2D MoS_2/C_3N_4 heterostructure by incorporating MoS_2 into C_3N_4, achieving an NH_3 yield of 18.5 μg h^{-1} mg_{cat}^{-1} and a high FE of 17.8% at −0.30 V *vs.* RHE in 0.1 mol/L $LiClO_4$ [162]. They attributed the enhanced performance to strong interfacial coupling between MoS_2 and C_3N_4, which stabilizes the $^*N_2H$ at Mo edge sites, lowers the entire reaction barrier, and protects the Mo active sites from competitive HER.

In addition to metal doping, non-metal incorporation is also highly effective in improving NRR activity. Jiang *et al.* reported a B-doped 3D carbon nitride electrocatalyst (B-UCN-X) with frustrated Lewis pairs, nitrogen defects and structural defects [163]. The B-UCN-15 sample achieved an NH_3 yield of 17.8 μg h^{-1} mg_{cat}^{-1} with an FE of 9.85% at −0.30 V *vs.* RHE in 0.1 mol/L Na_2SO_4. They confirmed that B-doping introduces cyanide groups and increases nitrogen defect density, thereby enhancing N_2 accessibility to active

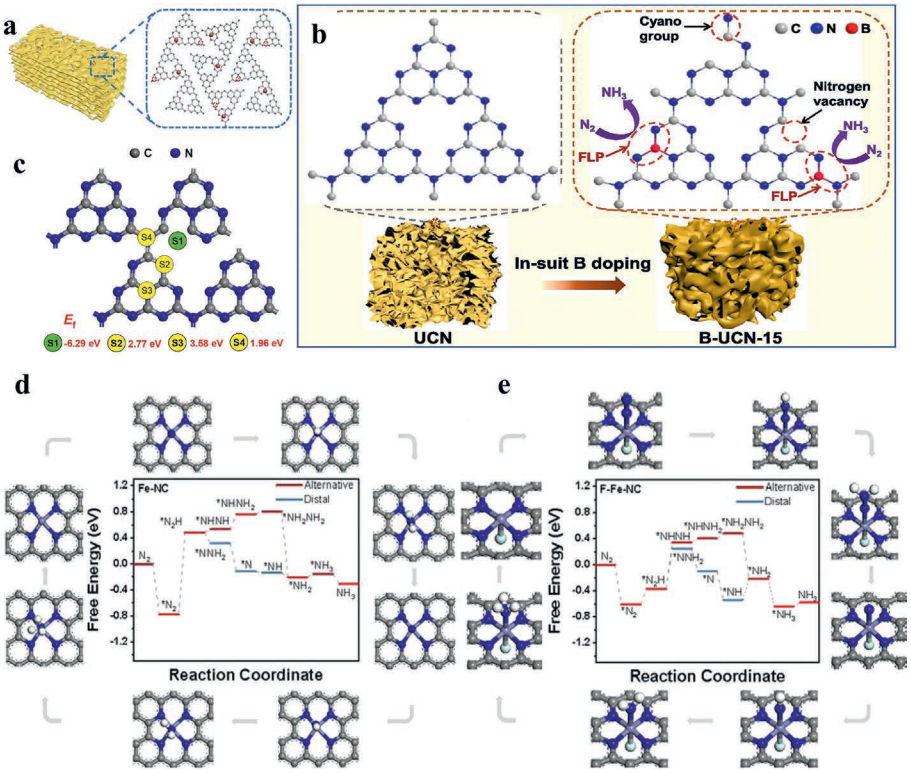


Fig. 9. (a) Schematic illustration of RuAu/Zr-C_3N_4 and its corresponding atomic structure for NRR. Reproduced with permission [161]. Copyright 2020, Elsevier. (b) Schematic diagram for the transformation of UCN to B-UCN-15. Copied with permission [163]. Copyright 2023, Elsevier. (c) Four possible S-doping sites in S-NV-C_3N_4 and corresponding formation energies (E_f). Reproduced with permission [164]. Copyright 2020, Elsevier. (d) Free energy diagram of the NRR with a distal and alternative pathway on Fe-NC. (e) Free energy diagram of the NRR with a distal and alternative pathway on F-Fe-NC. Reproduced with permission [165]. Copyright 2024, Elsevier.

sites (Fig. 9b). The Lewis acid synergistically promote N_2 adsorption/activation and suppress HER, achieving a high NH_3 yield. Regarding the stability of electrocatalysis, Chu *et al.* developed an efficient metal-free S-NV-C_3N_4 catalyst in which S doping stabilizes nitrogen vacancies by occupying energetically favorable substitution sites (Fig. 9c) [164]. This modification also significantly improves catalytic performance, yielding 32.7 μg h^{-1} mg_{cat}^{-1} NH_3 with an FE of 14.1 % at −0.40 V *vs.* RHE in 0.5 mol/L $LiClO_4$. DFT calculations revealed that S doping dramatically reduces the energy barrier for $^*NH_2$ to NH_3 conversion (from 1.13 eV to 0.18 eV) while retaining a favorable barrier for N_2 to $^*N_2H$ activation. This selective modulation of intermediate energetics enables more balanced adsorption of NRR intermediates and overall lower reaction barriers.

Similarly, metal and non-metal co-doping is a proven strategy for synergistic property enhancement. He *et al.* developed F-Fe-NC catalysts by dispersing atomically high-density Fe sites on N-doped carbon (Fe-NC) *via* CVD followed by fluorination [165]. The optimized F-Fe-NC exhibited an impressive NH_3 yield of 125.49 μg h^{-1} mg_{cat}^{-1} and an FE of 25.19 % in 0.1 mol/L Na_2SO_4. Fluorination effectively modulated the electronic configuration of Fe active sites, as reflected by the significant elongation of the N≡N bond (1.310 Å on F-Fe-NC *vs.* 1.210 Å on Fe-NC). Correspondingly, DFT calculations showed a substantially reduced potential-determining step energy barrier of 0.62 eV for F-Fe-NC, compared with 1.26 eV for Fe-NC (Figs. 9d and e).

In summary, metal, non-metal, or co-doping can effectively modulate the electronic structure of carbon nitride, disrupt structural symmetry, and generate defect-mediated active sites. These strategies collectively transform intrinsically inert carbon nitride into a highly efficient class of NRR catalysts.

5.5.3. Boron-based catalysts

Owing to their electron-deficient nature, boron-based materials exhibit a strong ability to activate N_2 molecules during the NRR, making them one of the most important classes of non-metallic NRR catalysts. In this section, we mainly focus on two representative boron-containing catalysts, namely BN- and BCN-based systems [166–168]. Some boron-doped catalysts have already been discussed in the “Carbon-based” and “Carbon-nitrogen catalysts” sections.

Numerous studies have demonstrated the potential of layered BN nanomaterials in electrochemical NRR [169–171]. However, their intrinsically wide band gap severely limits electronic transport. Carbon (C) doping has emerged as an effective strategy to modulate the bandgap of BN nanosheets and enhance their electrical transport properties. For instance, Liu *et al.* synthesized carbon-doped BN (C-BN) nanosheets with a highly porous lamellar structure (Fig. 10a) [172]. The unsaturated B atoms at the edge of these pores actively participate in the electrocatalytic NRR process. Moreover, the incorporation of C enhances electrical conductivity and facilitates faster electron transfer. As a result, the C-BN nanosheets achieved an exceptional NH_3 yield of 36.7 μg h^{-1} mg_{cat}^{-1} at −0.55 V *vs.* RHE with an FE of 6.51 %, representing a significant advancement in NRR performance. Similarly, Li *et al.* investigated intrinsic and carbon-doped hexagonal boron nitride nanoribbons (BNNRs) and demonstrated that C-doping significantly reduces the NRR overpotential from 1.14 V to 0.39 V [173]. The enhanced activity originates from carbon-induced charge redistribution around the edge B atoms induced by carbon incorporation, which promotes efficient N_2 activation and optimizes the reaction pathway by selectively modulating the adsorption strength of key intermediates (Fig. 10b).

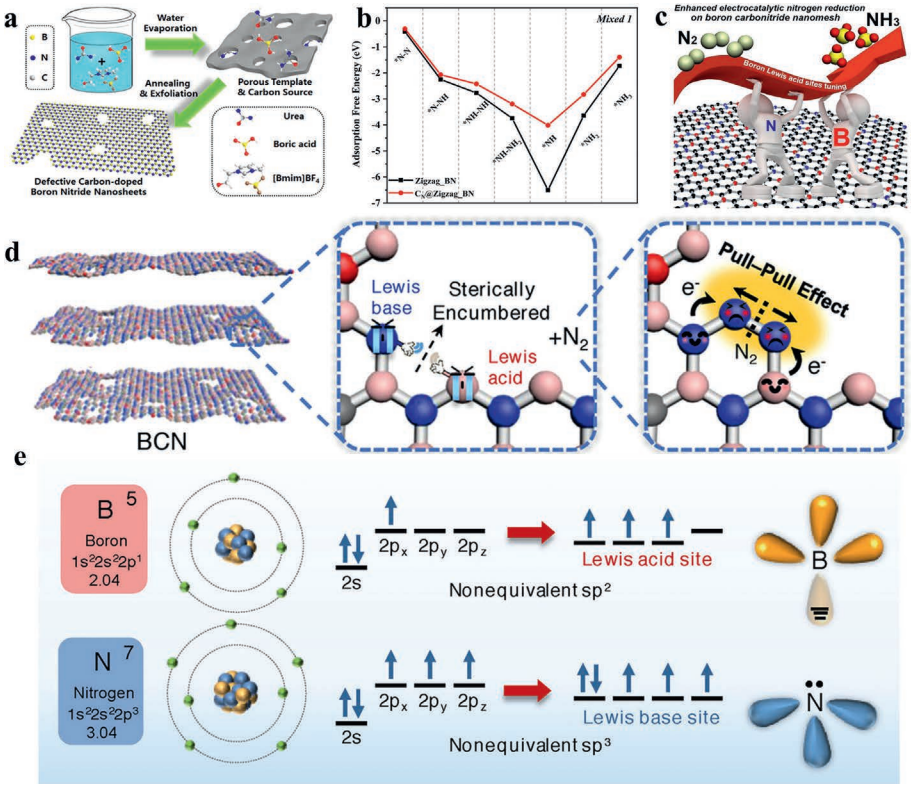


Fig. 10. (a) Schematic illustration for the stepwise synthesis of defective C-BN nanosheets. Reproduced with permission [172]. Copyright 2020, American Chemical Society. (b) The adsorption free energy line chart of the intermediates in the hydrogenation of N_2 adsorbed on the edge B atoms at pristine and C-doped zigzag BNNRs. Reproduced with permission [173]. Copyright 2021, Elsevier. (c) Schematic diagram of catalysis for BCN materials. Reproduced with permission [174]. Copyright 2020, Elsevier. (d) Schematic illustration of BCN for NRR (e) Sp^2 hybridization diagram of B element and sp^3 hybridization diagram of N element. Reproduced with permission [175]. Copyright 2022, Wiley-VCH GmbH.

Compared with C-BN, BCN exhibits a more uniform and tunable structure capable of forming numerous stable active sites for NRR. For example, Chang *et al*. designed a series of BCN materials with varying B/N atomic ratios and found that B-rich BCN (B-BCN) showed the best NRR performance [174]. It reached a maximum NH_3 yield of 41.9 μg h^{-1} mg_{cat}^{-1} with an FE of 9.87 % at −0.60 V *vs*. RHE in 0.05 mol/L Na_2SO_4. They confirmed that the electrons from boron atoms in B-rich domains transfer to adjacent N and C atoms, resulting in a localized positive charge distribution around boron atoms and an electron-deficient environment that strongly facilitates N_2 adsorption and activation (Fig. 10c). Similarly, Lin *et al*. synthesized high-purity BCN catalysts with abundant defective B/N sites through high-temperature annealing of $NaBH_4$, $NaNH_2$, and mesoporous carbon [175], followed by inorganic salt modification (Fig. 10d). The resulting catalyst features complementary active centers: Electron-deficient sp^2-hybridized B atoms (Lewis-acid sites) with unsaturated orbitals and empty p_z orbitals, and electron-rich sp^3-hybridized N atoms (Lewis-base sites). These sites cooperatively form sterically hindered N_2 traps, where a synergistic dual-site interaction drives exceptional NRR performance, achieving an NH_3 yield of 20.9 μg h^{-1} mg_{cat}^{-1} and an FE of 18.9 % (Fig. 10e).

In summary, carbon doping serves as a crucial strategy for modulating the electronic structure, improving electrical conductivity, and constructing stable active sites in BN materials. The introduction of carbon, or precise control over the B/N/C ratio, effectively promotes charge redistribution, optimizes intermediate adsorption, and reduces reaction overpotentials, leading to substantially enhanced catalytic performance.

5.5.4. Covalent organic framework catalysts

COFs feature ordered pore structures, high porosity, and exceptional chemical/thermal stability, making them ideal platforms for applications such as gas storage, sensing, proton conduction, and energy storage. Leveraging their high porosity, large surface area, and stability, COFs have recently emerged as promising electrocatalysts. In particular, the rational construction of active catalytic sites *(e.g.*, boron, metal sites, tailored functional groups) within COFs can significantly enhance the catalytic activity toward NH_3 synthesis.

Exploiting the inherent electron-deficient nature of boron, boron-containing COFs effectively combine electron-deficiency active centers with highly porous frameworks, ideally meeting the requirements for nitrogen fixation catalysts. For example, Liu *et al*. reported an electrochemically excited B-rich COFs (E_{ex}-COF), which achieved an NH_3 yield of 13 μg h^{-1} mg_{cat}^{-1} and an FE of 45.43 % in 0.1 mol/L KOH at −0.20 V *vs*. RHE [176]. The B sites in the COF readily interact with nitrogen species to form B-N bonds, inducing lattice distortion and enhancing the its affinity toward N_2 adsorption and activation. Relative to the pristine COFs, E_{ex}-COF displays a higher density of active sites with strong N_2 affinity, establishing a self-sustaining cycle that progressively optimizes the catalytic state (Fig. 11a).

Incorporating highly stable and conductive transition metals into COFs provides another effective strategy to enhance NRR performance. Wang *et al*. screened 20 conductive 2D TM-COFs (TM = Sc, Ti, V, Cr, Mn, Fe, Co, Ni, Cu, Zn, Nb, Mo, Ru, Rh, Pd, Ag, W, Ir, Pt, Au) linked by phthalocyanine-pyrene units and identified Mo-COF as the best catalyst [177]. At an overpotential of 0.16 V, Mo-COF can effectively suppress the HER while accelerat-

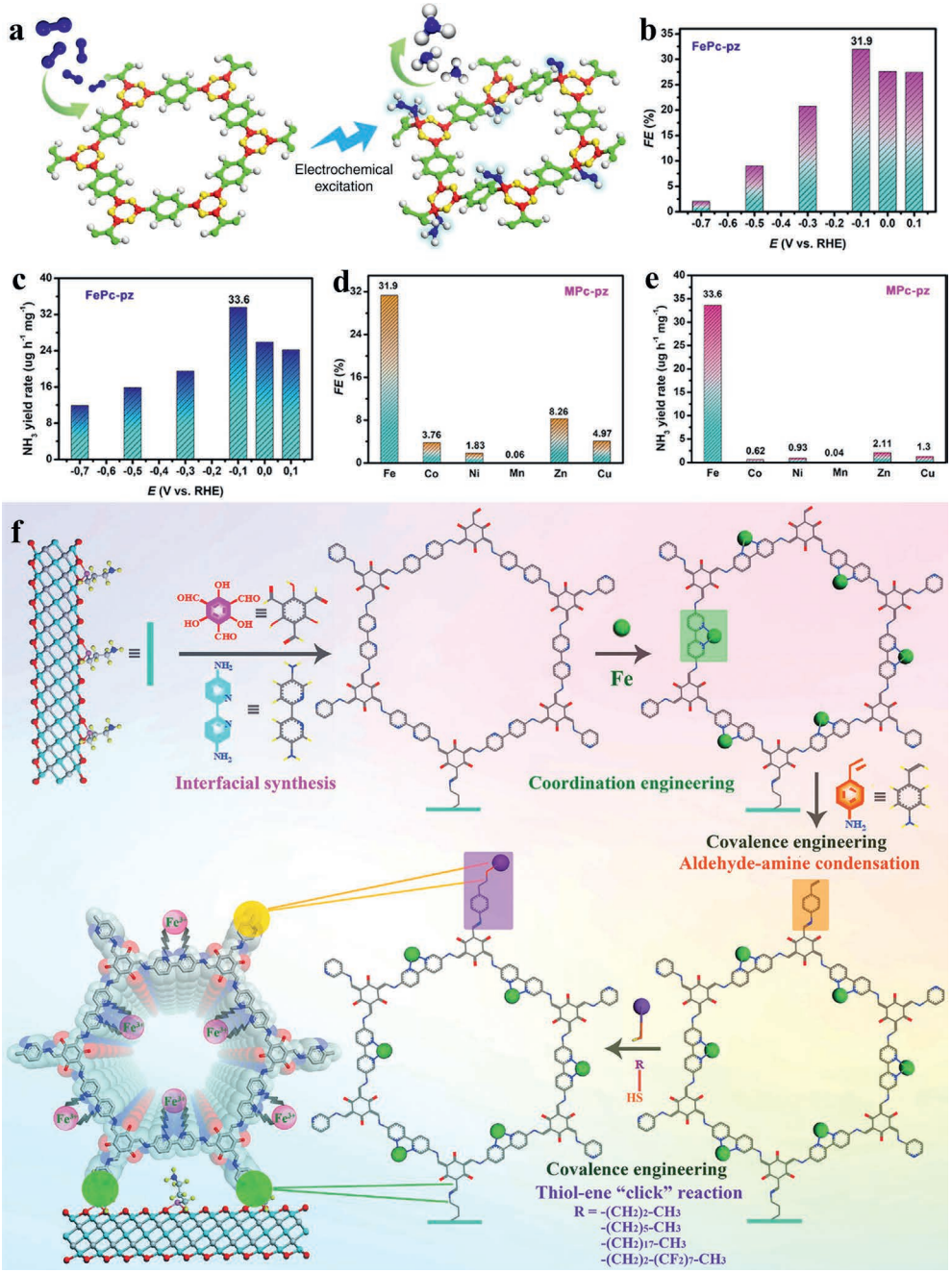


Fig. 11. (a) Schematic illustration of the electrochemical excitation of COF. Reproduced with permission [176]. Copyright 2019, The Author(s). (b, d) FE and (c, e) NH_3 yield rate of FePc-pz and MPc-pz (M = Fe, Co, Ni, Mn, Cu, and Zn) under different electrolysis potentials, respectively. Reproduced with permission [178]. Copyright 2021, American Chemical Society. (f) Schematic diagram of the synthesis of hydrophobic COF-Fe/MXene nanosheets. Reproduced with permission [179]. Copyright 2023, Wiley-VCH GmbH.

ing the NRR pathway and lowering the energy barrier for N_2 to NH_3 conversion. Subsequently, Zhong *et al.* further optimized the active site configuration by developing 2D conjugated COFs with M-Nx-C-centers, based on FePc-pyrene units linked by pyrazine bonds [178]. Comparative studies across different metal centers revealed that the FePc-pz framework showed the best performance, achieving an NH_3 yield of 33.6 μg h^{-1} mg_{cat}^{-1} and an FE of 31.9 % at −0.10 V *vs.* RHE in 0.01 mol/L H_2SO_4 (Figs. 11b–e). This superior activity was attributed to the localized Fermi-level states of Fe, which facilitates N_2 adsorption through strong binding interactions, lower activation barriers and promote NRR kinetics.

Hydrophobicity engineering *via* functional group modulation offers an alternative pathway to improve catalytic selectivity and efficiency. He *et al.* engineered hydrophobic COF-Fe/MXene nanosheets modified with perfluorododecane thiol, creating a hydrophilic-to-superhydrophobic gradient interface by tailoring the ratio of -F to -OH terminal groups on the MXene surface [179]. This design effectively repels aqueous electrolytes while enhancing N_2 adsorption. Benefiting from the synergistic effects of hydrophobicity and Fe active sites, the catalyst achieved an NH_3 yield of 41.8 μg h^{-1} mg_{cat}^{-1} and an FE of 43.1 % at −0.50 V *vs.* RHE (Fig. 11f). Similarly, Wang *et al.* engineered fluorinated olefin-linked COFs *via* a cosolvent strategy to ensure high crystallinity, porosity, and expanded surface area [180]. The introduction of fluorine endowed NKCOF-17 with strong hydrophobicity, effectively suppressing the HER. When used as a support for Pd nanoparticles, NKCOF-17 prevented metal ag-

Table 6
Types and properties of representative nonmetallic-based catalysts.[a]

Electrocatalyst	Electrolyte	Potential (V *vs.* RHE)	Yield rate of NH_3 ($\mu g\ h^{-1}\ mg_{cat}^{-1}$)	FE (%)	Ref.
Oxidized carbon	0.05 mol/L H_2SO_4	−0.50/−0.30	32.20	16.5	[152]
BG	0.05 mol/L H_2SO_4	−0.50	9.80	10.8	[155]
P-G	0.5 mol/L $LiClO_4$	−0.50	32.33	20.8	[156]
Fe-B/N-C	0.1 mol/L Na_2SO_4	−0.40	100.10	23.0	[157]
Zr-C_3N_4	0.1 mol/L KOH	−0.10	5.28	11.5	[161]
MoS_2/C_3N_4	0.1 mol/L $LiClO_4$	−0.30	18.50	17.8	[162]
B-UCN-15	0.1 mol/L Na_2SO_4	−0.30	17.80	9.9	[163]
S-NV-C_3N_4	0.5 mol/L $LiClO_4$	−0.40	32.70	14.1	[164]
F-Fe-NC	0.1 mol/L Na_2SO_4	−0.25	125.49	25.2	[165]
C-BN	0.1 mol/L HCl	−0.55	36.70	6.5	[172]
B-BCN	0.05 mol/L Na_2SO_4	−0.60	41.90	9.9	[174]
BCN	0.5 mol/L H_2SO_4	−0.40/−0.10	20.90	18.9	[175]
E_{ex}-COF	0.1 mol/L KOH	−0.20	13.00	45.4	[176]
FePc-pz	0.01 mol/L H_2SO_4	−0.10	33.60	31.9	[178]
COF-Fe/MXene	0.1 mol/L Na_2SO_4	−0.50	41.80	43.1	[179]
Pd/NKCOF-17	0.1 mol/L Na_2SO_4	−0.20	90.26	44.0	[180]

[a] Testing condition: room temperature/atmospheric pressure; N_2 flow rate (about 20 mL/min).

glomeration and enhanced active-site dispersion and stability, enabling an NH_3 yield of 90.26 $\mu g\ h^{-1}\ mg_{cat}^{-1}$ and an FE of 44% at −0.20 V *vs.* RHE in 0.1 mol/L Na_2SO_4.

In summary, the application of COFs in NRR mainly involves three key modification strategies: the construction of boron-based electron-deficient centers, the integration of transition metals, and hydrophobicity engineering. These approaches significantly enhance catalytic activity and selectivity by regulating the electronic structure, optimizing the density and distribution of active sites, suppressing the competitive HER, and promoting N_2 adsorption and activation. Finally, the representative non-metal-based NRR catalysts discussed in this review, along with their corresponding performance metrics, are systematically compared and summarized in Table 6.

6. Comparison of electrocatalysts for NRR

Based on the introduction of the various catalysts mentioned above, we have systematically reviewed their developmental progress. In fact, each category of catalyst exhibits distinct advantages and limitations, as well as unresolved challenges that require further investigation. Accordingly, this section summarizes the advantages and disadvantages of the major catalyst classes and outlines corresponding improvement strategies, as presented in Table 7.

A comparative analysis of these catalysts reveals a strong interdependence between the electrocatalytic reaction pathway and catalyst identity. As the reaction core, the catalyst governs N_2 adsorption modes and the stability of key intermediate through its active site geometry, electronic structure, and local microenvironment, thereby determining the specific NRR pathway [20,181,182].

Specifically, the geometric configuration of active sites plays a key role in controlling N_2 adsorption. Asymmetric or undercoordinated sites favor tilted end-on adsorption, thereby promoting the distal pathway, whereas symmetric or binuclear sites facilitate side-on adsorption with comparable activation of both N atoms, favoring the alternating pathway. In parallel, electronic structure effects further modulate pathway selectivity. High d-band centers can strongly activate the N≡N bond but require appropriate geometric matching to prevent overbinding. Moderate d-band centers optimize the intermediate adsorption energies and, when combined with symmetric geometries, synergistically promote the alternating pathway, whereas electron-deficient centers enable differential N_2 activation *via* lone-pair acceptance. Moreover, although the reaction microenvironment does not alter the intrinsic reaction pathway, it significantly influences hydrogenation kinetics and competition with the HER, thereby affecting practical catalytic efficiency. Therefore, the rational design of highly selective NRR catalysts relies on the synergistic modulation

Table 7
Comparison of electrocatalysts and strategies for improving NRR properties.

Electrocatalysts	Advantages	Disadvantages	Strategies for improving NRR properties
Noble metal catalysts	High intrinsic activity; Superior electrical conductivity; Excellent corrosion resistance; High thermal stability	Prohibitive cost; Elemental scarcity	Constructing nanoporous architectures; Anchoring on highly active non-metallic substrates
Transition metals catalysts	Low costs; Diversified categories	Poor stability at high temperature/potential; Severe side reactions	Creating electron-deficient sites by heteroatom doping; Vacancy engineering enables superior N_2 chemisorption activity
Single atom catalysts	High atomic utilization; Strong metal-support interactions; Exceptional reaction selectivity	Compromised stability/activity	Optimization of synergistic effects *via* defect-tailored supports enables an aggregation-free isolated atomic distribution
MOFs	High specific surface area and abundant pore channels; Precisely designed active sites; Modulation of the catalytic environment	Poor stability; Dependence on modification	Enhancement of electrical conductivity; Selection of stable metal nodes and ligands; Fabrication of ultrathin two-dimensional nanosheets
Nonmetallic-based catalysts	Effective suppression of HER; Tunable frameworks; Low costs	Challenges in creating high-density active sites; Stringent synthesis conditions; Poor electrical conductivity; Sparse active sites	Hierarchical structural design; Strategic heteroatom doping; Hybrid composite construction

Table 8
Summary of the relationships between catalysts and reaction pathways.

Dominant factors	Specific characteristics	Effect on N_2 adsorption and activation	NRR pathways	Regulation methods
Site geometry	Asymmetric or single site	End-on N_2 adsorption	Distal	Constructing single-atom catalysts; Creating defects and vacancies
	Symmetric or double site	Side-on N_2 adsorption, equal activation of N atoms	Alternating	Constructing dual-atom catalysts; Designing MOFs catalysts; Adjusting atomic spacing on supports
Electronic structure	High d-band center	Strong electron feedback significantly weakens N≡N bond, thereby leading to strong adsorption or dissociation	Distal or alternating	Heteroatom doping; Adjusting ligand environment; Changing lattice dimensions
	Moderate d-band center	Optimizes adsorption energy of various intermediates, avoiding overly strong or weak adsorption	Favors alternating	
	Electron-deficient	Acts as Lewis acid to accept lone pair electrons from N_2	Distal or alternating	Constructing charge transfer interfaces; Introducing electron-withdrawing/donating groups
Microenvironment	Hydrophilic or proton-rich	Accelerates hydrogenation steps but severely intensifies HER competition	Does not directly determine reaction pathway	Designing surface functional groups; Selecting suitable supports
	Hydrophobic or proton-deficient	Suppresses HER but may limit proton supply		

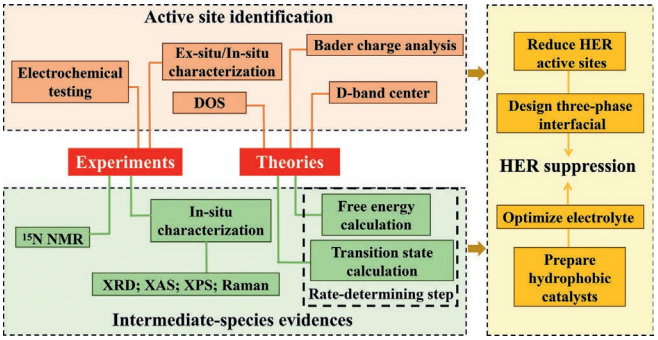


Fig. 12. Strategies for HER suppression and identification of active sites, key intermediates, and the rate-determining steps.

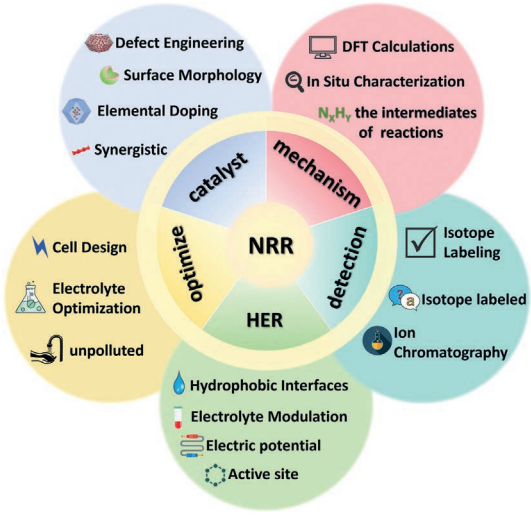


Fig. 13. Summary of performance-enhancing strategies for the NRR, highlighting the necessity of multi-dimensional synergistic modulation for significant improvement.

of geometric configuration and electronic structure to efficiently direct the reaction along the target pathway.

Based on this framework, the relationships between catalysts and reaction pathways are summarized in Table 8. And the corresponding strategies for HER-suppression and identification of active sites, key intermediates, and the rate-determining steps are illustrated in Fig. 12.

7. Conclusion and prospect

In conclusion, this review summarizes reaction pathways, fundamental mechanisms, electrolytic cells, and NH_3 detection methods, and comprehensively surveys recent advances in electrocatalysts while systematically discussing optimization strategies across different material classes, as shown in Fig. 13. Overall, the NRR offers a highly efficient, low-energy, and sustainable alternative to the traditional H–B process and has achieved substantial progress in recent years. Nevertheless, this technology remains at an early developmental stage, primarily constrained by persistently low FE (typically below 50%) and insufficient NH_3 yield, which together constitute the main barriers to industrial application. Moreover, catalyst synthesis is largely confined to laboratory-scale production and suffers from high manufacturing costs. In addition, the active sites of current catalysts often fail to maintain long-term stability over thousands of hours of operation, severely compromising the economic feasibility and industrial scalability of electrocatalytic NRR. Consequently, intensified research efforts are urgently required. Based on the above review, future perspectives are proposed with respect to catalyst design, reaction mechanisms, HER suppression, electrolyte and electrochemical cell optimization, and reliable NH_3 quantification, with the aim of offering guidance and direction for further advancement in this field.

(1) *Optimizing catalyst structures and compositions.* Significant advances in NRR catalyst design have attracted extensive research interest. Nevertheless, most currently developed catalysts remain constrained by inherent limitations, as research has predominantly focused on microstructural modifications. Future efforts should emphasize rational structural modulation, including surface morphology engineering, defect and vacancy construction, and atomic-scale lattice defect modulation, to maximize the exposure and accessibility of active sites. Meanwhile, synergistic enhancement through heteroatom doping and co-doping can effectively tune the adsorption energetics of N_2 and key reaction intermediates, thereby boosting intrinsic catalytic activity and selectivity.

(2) *Advancing theoretical calculations and characterization techniques for NRR mechanisms.* DFT calculations method play a crucial role in elucidating adsorption energetics, reaction thermodynamics, overpotentials, and rate-determining steps during the NRR process [183]. However, the conversion of N_2 to NH_3 involves multiple complex intermediates, and theoretical predictions alone are insufficient to fully unravel the reaction mechanism. Therefore, future

studies should integrate advanced *in situ* characterization techniques *(e.g.*, mass spectrometry, infrared spectroscopy, X-ray photoelectron spectroscopy, Raman spectroscopy) to directly identify authentic active sites, monitor intermediate species, clarify dynamic surface evolution under working conditions [184].

(3) *Suppressing the competing HER.* NRR inevitably competes with the hydrogen evolution reaction, as both processes often occur on the same active sites. To effectively promote the electrocatalytic nitrogen fixation, targeted strategies must be implemented to suppress the dominant HER. These include tailoring catalyst selectivity through electronic structure modulation and active site engineering, optimizing electrolyte systems *via* pH control and proton donor concentration regulation, and precisely regulating operational parameters such as applied potential and mass transport. By introducing thermodynamic barriers and kinetic proton-suppression mechanisms, reaction selectivity can be fundamentally shifted toward N_2 to NH_3 synthesis.

(4) *Selecting optimal electrolytes and electrochemical cells.* Although catalyst design has become a central research focus for improving NRR performance, treating it as a standalone strategy may restrict further development. Future NRR systems should adopt an integrated design approach that combines advanced catalysts with optimized electrochemical cells and electrolytes. For gas-proton-coupled electrolysis systems, the development of dual-chamber cells is highly desirable. Constructing three-phase interfaces at the cathode can enhance N_2 adsorption and activation, while hydrophobic Nafion membranes may effectively modulate wetting behavior and suppress HER. Regarding electrolytes, ionic solutions with high N_2 solubility and reduced proton activity (*e.g.*, $LiClO_4$, K_2SO_4) are advantageous for improving NRR selectivity. Furthermore, the pH of the electrolyte directly affects surface charge states and adsorption capabilities of intermediates, thereby influencing NRR activity. Finally, it is essential to ensure the cleanliness of the catalytic reaction process, including the working-electrode clip, counter electrode, reference electrode, and electrolyte.

(5) *Ensuring accurate quantification methods for* NH_3 *products.* Reliable quantification of NH_3 and N_2H_4 is crucial for accurately evaluating FE and NH_3 yield in electrocatalytic systems. Moreover, NH_3 contamination is ubiquitous in laboratory environments and chemical reagents, making precise source identification and contamination control indispensable. To address the shortcomings of conventional UV–vis colorimetry, future studies should integrate complementary techniques such as ion-selective electrodes, ion chromatography, and isotope-labeling methods. Combining these approaches can significantly enhance sensitivity, accuracy, and overall reliability. Given that all detection methods possess inherent limitations and may introduce systematic errors under certain conditions, comprehensive cross-validation and comparative analysis are essential for selecting the most appropriate quantification strategy for specific experimental systems.

CRediT authorship contribution statement

Jie Hou: Writing – original draft, Conceptualization. **Bin Liu:** Writing – review & editing, Supervision, Funding acquisition, Conceptualization. **Wenjing Zheng:** Writing – review & editing, Supervision. **Yaling Wang:** Writing – review & editing, Supervision. **Guangqun Cao:** Supervision. **Shengliang Hu:** Supervision.

Declaration of competing interest

The authors declare that they have not any commercial or associative interest that represents a conflict of interest in connection with the work submitted.

Acknowledgments

We gratefully acknowledge the financial support from the National Natural Science Foundation of China (No. 52302051), the Foundational Research Project of Shanxi Province (No. 202303021221115, 202203021221108), and the Science and Technology Innovation Teams of Shanxi Province (No. 202304051001014).

References

[1] Y. Pang, C. Su, L. Xu, Z. Shao, Prog. Mater. Sci. 132 (2023) 101044.
[2] X. Zhang, E.A. Davidson, D.L. Mauzerall, et al., Nature 528 (2015) 51–59.
[3] Z. Shu, Y. Cai, J. Mater. Chem. A 9 (2021) 16056–16064.
[4] Y. Wan, J. Xu, R. Lv, Mater. Today 27 (2019) 69–90.
[5] Y. Lv, Y. Wang, M. Yang, et al., J. Mater. Chem. A 9 (2021) 1480–1486.
[6] J. Deng, J.A. Iñiguez, C. Liu, Joule 2 (2018) 846–856.
[7] X. Feng, J. Liu, L. Chen, et al., J. Am. Chem. Soc. 145 (2023) 10259–10267.
[8] W. Song, L. Yue, X. Fan, et al., Inorg. Chem. Front. 10 (2023) 3489–3514.
[9] M.A. Mushtaq, M. Arif, G. Yasin, et al., Renew. Sustain. Energy Rev. 176 (2023) 113197.
[10] S.L. Meng, X.B. Li, C.H. Tung, L.Z. Wu, Chem 7 (2021) 1431–1450.
[11] Y. Wei, W. Jiang, Y. Liu, et al., Nanoscale 14 (2022) 2990–2997.
[12] K. Hu, P. Qiu, L. Zeng, et al., Angew. Chem. Int. Ed. 59 (2020) 20666–20671.
[13] L. Pospíšil, M. Hromadová, M. Gál, et al., Electrochim. Acta 53 (2008) 7445–7450.
[14] X. Guo, H. Du, F. Qu, J. Li, J. Mater. Chem. A 7 (2019) 3531–3543.
[15] C. Lv, Y. Qian, C. Yan, et al., Angew. Chem. Int. Ed. 57 (2018) 10246–10250.
[16] X. Wang, X. Li, A. Guo, W. Luo, W. Yang, J. Alloys Compd. 1014 (2025) 178680.
[17] J. Wang, Z. Huang, J. Chen, et al., Can. J. Chem. Eng. 104 (2026) 2365–2376.
[18] X. Li, X. Wang, A. Guo, et al., J. Colloid Interface Sci. 678 (2025) 1143–1152.
[19] Y. Cao, S. Yuan, L. Meng, et al., ACS Sustain. Chem. Eng. 11 (2023) 7965–7985.
[20] W. Tan, H. Zhao, L. Ding, et al., ACS Appl. Nano Mater. 8 (2025) 2632–2651.
[21] J. Lai, T. Li, L. Ding, G. Chen, H. Wang, ChemSusChem 18 (2025) e202401912.
[22] D. Liu, M. Chen, X. Du, et al., Adv. Funct. Mater. 31 (2021) 2008983.
[23] J. Hu, H. Zou, F. Li, et al., Energy Fuels 37 (2023) 3501–3522.
[24] J.G. Chen, R.M. Crooks, L.C. Seefeldt, et al., Science 360 (2018) eaar6611.
[25] X. Cui, C. Tang, Q. Zhang, Adv. Energy Mater. 8 (2018) 1800369.
[26] Y. Huang, D.D. Babu, Z. Peng, Y. Wang, Adv. Sci. 7 (2020) 1902390.
[27] X.F. Li, Q.K. Li, J. Cheng, et al., J. Am. Chem. Soc. 138 (2016) 8706–8709.
[28] H. He, H.K. Li, Q.Q. Zhu, et al., Appl. Catal. B: Environ. 316 (2022) 121673.
[29] R. Zhang, H. Guo, L. Yang, et al., ChemElectroChem 6 (2019) 1014–1018.
[30] K. Cheng, S. Li, Q. Cheng, et al., Adv. Funct. Mater. 35 (2025) 2417914.
[31] C. Li, T. Wang, Z. Zhao, et al., Angew. Chem. Int. Ed. 57 (2018) 5278–5282.
[32] R. Lan, J.T.S. Irvine, S. Tao, Sci. Rep. 3 (2013) 1145.
[33] D. Bao, Q. Zhang, F. Meng, et al., Adv. Mater. 29 (2017) 1604799.
[34] Y. Sun, B. Xia, S. Ding, et al., J. Mater. Chem. A 9 (2021) 20040–20047.
[35] L. Zuo, H. Yang, H. Li, et al., Adv. Funct. Mater. 36 (2026) e19261.
[36] F. Köleli, T. Röpke, Appl. Catal. B: Environ. 62 (2006) 306–310.
[37] M.A. Shipman, M.D. Symes, Catal. Today 286 (2017) 57–68.
[38] Y. Li, Y. Ji, Y. Zhao, et al., Adv. Mater. 34 (2022) 2202240.
[39] S.Z. Andersen, V. Čolić, S. Yang, et al., Nature 570 (2019) 504–508.
[40] H. Zou, W. Rong, S. Wei, Y. Ji, L. Duan, Proc. Natl. Acad. Sci. U. S. A. 117 (2020) 29462–29468.
[41] S. Chen, S. Perathoner, C. Ampelli, et al., Angew. Chem. Int. Ed. 56 (2017) 2699–2703.
[42] D.H. Thomas, M. Rey, P.E. Jackson, J. Chromatogr. A 956 (2002) 181–186.
[43] J. Liu, M.S. Kelley, W. Wu, et al., Proc. Natl. Acad. Sci. U. S. A. 113 (2016) 5530–5535.
[44] Y. Zhao, F. Wu, Y. Miao, et al., Angew. Chem. Int. Ed. 60 (2021) 21728–21731.
[45] Y. Zhao, R. Shi, X. Bian, et al., Adv. Sci. 6 (2019) 1802109.
[46] L. Zhou, C.E. Boyd, Aquaculture 450 (2016) 187–193.
[47] R.Y. Hodgetts, A.S. Kiryutin, P. Nichols, et al., ACS Energy Lett. 5 (2020) 736–741.
[48] Y. Zhu, D. Yuan, H. Lin, T. Zhou, Anal. Lett. 49 (2016) 665–675.
[49] A. LeDuy, R. Samson, Biotechnol. Lett. 4 (1982) 303–306.
[50] N. Furuya, H. Yoshiba, J. Electroanal. Chem. Interfacial Electrochem. 291 (1990) 269–272.
[51] Y. Liu, L. Huang, X. Zhu, Y. Fang, S. Dong, Nanoscale 12 (2020) 1811–1816.
[52] W. Tong, B. Huang, P. Wang, Q. Shao, X. Huang, Natl. Sci. Rev. 8 (2021) nwaa088.
[53] Y.C. Jiang, Y.J. Mao, J. Zou, et al., Chem. Commun. 56 (2020) 12254.
[54] H. Zhao, D. Zhang, H. Li, et al., Adv. Energy Mater. 10 (2020) 2002131.
[55] Y. Yang, J. Liu, M. Zhang, et al., Nano Res. 18 (2025) 94907274.
[56] M. Zhang, Y. Zhao, G. Li, et al., Chin. Chem. Lett. 37 (2026) 111181.
[57] Z. Wang, Y. Li, H. Yu, et al., ChemSusChem 11 (2018) 3480–3485.
[58] P. Wang, Y. Ji, Q. Shao, Y. Li, X. Huang, Sci. Bull. 65 (2020) 350–358.
[59] D. Chen, M. Luo, S. Ning, et al., Small 18 (2022) 2104043.
[60] G. Deng, T. Wang, A.A. Alshehri, et al., J. Mater. Chem. A 7 (2019) 21674–21677.
[61] F. Pang, Z. Wang, K. Zhang, et al., Nano Energy 58 (2019) 834–841.
[62] B. Chang, H. Yuan, L. Li, et al., Appl. Catal. B: Environ. 320 (2023) 121777.
[63] H.M. Liu, S.H. Han, Y. Zhao, et al., J. Mater. Chem. A 6 (2018) 3211–3217.

[64] W. Song, Z. Fu, P. Ma, et al., Appl. Surf. Sci. 617 (2023) 156550.
[65] H. Kong, P. Ma, W. Zhang, M. Jia, W. Song, Mater. Chem. Phys. 297 (2023) 127396.
[66] X. Long, F. Huang, Z. Yao, et al., Small 20 (2024) 2400551.
[67] Y. Wu, C. He, W. Zhang, ACS Appl. Mater. Interfaces 13 (2021) 47520–47529.
[68] S.Y. Park, Y.J. Jang, D.H. Youn, Catalysts 13 (2023) 639.
[69] A. Rasool, M.A. Dar, Catal. Sci. Technol. 14 (2024) 5687–5698.
[70] L. Zhao, B. Chang, T. Dong, et al., J. Mater. Chem. A 10 (2022) 20071–20079.
[71] D. Johnson, A. Djire, Adv. Mater. Interfaces 10 (2023) 2202147.
[72] Y. Yang, C. Hu, J. Shan, et al., Angew. Chem. Int. Ed. 62 (2023) e202300989.
[73] H. Yang, F. Wang, H. Zhang, et al., J. Am. Chem. Soc. 142 (2020) 4438–4444.
[74] Y. Zhao, Q. Liu, B. Zhou, G. Yang, S. Jiang, Rare Met. 43 (2024) 5860–5867.
[75] S. He, F. Shen, J. Zou, et al., Chin. Chem. Lett. 37 (2026) 111397.
[76] C. Fu, L. Luo, L. Yang, et al., J. Phys. Chem. C 125 (2021) 17051–17057.
[77] A. Allangawi, N. Kosar, K. Ayub, et al., Phys. Scr. 99 (2024) 105023.
[78] H. Bu, J. Shao, J. Ma, H. Gao, J. Phys. Chem. C 127 (2023) 17742–17753.
[79] Y. Kong, C. Lv, G. Chen, Mater. Today Energy 31 (2023) 101215.
[80] L. Hui, Y. Xue, H. Yu, et al., J. Am. Chem. Soc. 141 (2019) 10677–10683.
[81] Y. Ren, C. Yu, X. Song, et al., J. Mater. Chem. A 9 (2021) 13036–13043.
[82] B. Chang, Z. Cao, Y. Ren, et al., ACS Nano 18 (2024) 288–298.
[83] Y. Liu, L. Tang, J. Dai, J. Yu, B. Ding, Angew. Chem. Int. Ed. 59 (2020) 13623–13627.
[84] X. Wang, Z. Kang, D. Wang, et al., Nano Energy 121 (2024) 109268.
[85] T. Li, J. Xia, H. Xian, et al., Int. J. Hydrog. Energy 47 (2022) 3550–3555.
[86] Y. Ji, Q. Hu, W. Cheng, X. Liu, A.C.S. Sustain, Chem. Eng. 12 (2024) 6806–6810.
[87] T. Takashima, H. Fukasawa, T. Mochida, H. Irie, ACS Appl. Nano Mater. 6 (2023) 23381–23389.
[88] S. Chen, S. Perathoner, C. Ampelli, et al., J. Energy Chem. 49 (2020) 22–32.
[89] Y. Wang, K. Jia, Q. Pan, et al., ACS Sustain. Chem. Eng. 7 (2019) 117–122.
[90] H. Xian, H. Guo, J. Xia, et al., ACS Appl. Mater. Interfaces 13 (2021) 7142–7151.
[91] M. Xie, F. Dai, H. Guo, et al., Adv. Energy Mater. 13 (2023) 2203032.
[92] H. Chen, J. Liang, L. Li, et al., ACS Appl. Mater. Interfaces 13 (2021) 41715–41722.
[93] J. Zhang, Y. Guo, H. Li, et al., Int. J. Miner. Metall. Mater. 32 (2025) 936–943.
[94] H. Yang, B. Qin, L. Zuo, et al., Adv. Funct. Mater. 36 (2026) e04057.
[95] J. Duan, R. Liu, M. Bian, et al., J. Alloys Compd. 991 (2024) 174537.
[96] G. Zhan, F. Quan, Y. Yao, et al., Appl. Catal. B: Environ. 323 (2023) 122186.
[97] H. Su, L. Chen, Y. Chen, et al., Angew. Chem. Int. Ed. 59 (2020) 20411–20416.
[98] Y. Zhao, Y. Zhao, R. Shi, et al., Adv. Mater. 31 (2019) 1806482.
[99] L. Tao, L. Huang, K. Pang, C. Li, H. Ji, Inorg. Chem. Commun. 145 (2022) 110003.
[100] K. Ba, G. Wang, T. Ye, et al., ACS Catal. 10 (2020) 7864–7870.
[101] X. Ren, G. Cui, L. Chen, et al., Chem. Commun. 54 (2018) 8474–8477.
[102] L. Zhang, X. Ji, X. Ren, et al., ACS Sustain. Chem. Eng. 7 (2019) 1807.
[103] H. Cheng, L. Ding, G. Chen, et al., Adv. Mater. 30 (2018) 1803694.
[104] L. Xu, L. Liu, G. Chen, D. Xia, Chin. Chem. Lett. 37 (2026) 111188.
[105] Z. Chen, Z. Zhang, Rare Met. 42 (2023) 1050–1055.
[106] Z.Y. Wu, M. Karamad, X. Yong, et al., Nat. Commun. 12 (2021) 2870.
[107] Y. Zhang, J.Z. Wang, K. Li, et al., J. Mater. Chem. A 10 (2022) 2819–2825.
[108] X. Zhang, X. Lin, X. Huang, et al., Carbon Fut. 1 (2024) 9200008.
[109] L. Tang, J. Dai, Y.T. Liu, et al., Compos. Commun. 23 (2021) 100551.
[110] F. Wang, Y. Wang, L. Li, et al., Int. J. Hydrog. Energy 48 (2023) 17677–17688.
[111] B. Qiao, A. Wang, X. Yang, et al., Nat. Chem. 3 (2011) 634–641.
[112] W. Zang, T. Yang, H. Zou, et al., ACS Catal. 9 (2019) 10166–10173.
[113] H. Tao, C. Choi, L.X. Ding, et al., Chem 5 (2019) 204–214.
[114] L. Yang, C. Cheng, X. Zhang, et al., Chin. J. Catal. 43 (2022) 3177–3186.
[115] P. Shen, X. Li, Y. Luo, et al., Appl. Catal. B: Environ. 316 (2022) 121707.
[116] Q. Li, X. Liu, M. Wang, Chem. Eng. J. 496 (2024) 154217.
[117] Y.H. Xiao, Z.W. Ma, T.R. Wu, et al., Mol. Catal. 585 (2025) 115323.
[118] C. He, D. Chen, S. Xi, W. Zhang, J. Mater. Chem. A 13 (2025) 16716–16727.
[119] M.A. Akhound, M. Soleimani, M. Pourfath, ACS Appl. Mater. Interfaces 17 (2025) 15385–15397.
[120] M. Yang, J. Yang, N. He, et al., ACS Appl. Nano Mater. 8 (2025) 179–188.
[121] S. Biswas, J. Zhou, X. Chen, et al., Angew. Chem. Int. Ed. 64 (2025) e202507947.
[122] T. Zhang, Z. Che, Y. Song, et al., Chin. Chem. Lett. 36 (2025) 111295.
[123] X. Li, P. Shen, Y. Luo, et al., Angew. Chem. Int. Ed. 61 (2022) e202205923.
[124] C. Kim, J. Song, C. Choi, et al., Adv. Mater. 34 (2022) 2205270.
[125] Q. Shi, M. Cheng, Y. Liu, et al., Coord. Chem. Rev. 499 (2024) 215500.
[126] G. Gao, X. Chen, L. Han, et al., Coord. Chem. Rev. 503 (2024) 215639.
[127] Y. Liu, Y. Shi, X. Xin, et al., Appl. Catal. B: Environ. Energy 363 (2025) 124815.
[128] Y. Abghoui, A.L. Garden, J.G. Howalt, T. Vegge, E. Skúlason, ACS Catal. 6 (2016) 635–646.
[129] X. Zhao, F. Yin, N. Liu, et al., J. Mater. Sci. 52 (2017) 10175–10185.
[130] X. Yi, X. He, F. Yin, et al., J. Mater. Sci. 55 (2020) 12041–12052.
[131] P.Y. Liu, K. Shi, W.Z. Chen, et al., Appl. Catal. B: Environ. 287 (2021) 119956.
[132] C. Yang, Y. Zhu, J. Liu, et al., Nano Energy 77 (2020) 105126.
[133] Y.X. Wang, C. Liu, Y.J. Chen, et al., Environ. Res. 161 (2018) 336–344.
[134] L. Wen, X. Li, R. Zhang, et al., ACS Appl. Mater. Interfaces 13 (2021) 14181–14188.
[135] D.Y. Wang, M. Gong, H.L. Chou, et al., J. Am. Chem. Soc. 137 (2015) 1587–1592.
[136] S. Luo, X. Li, W. Gao, H. Zhang, M. Luo, Sustain. Energy Fuels 4 (2020) 164–170.
[137] L. Huang, L. Tao, K. Pang, et al., Catal. Sci. Technol. 13 (2023) 3629–3637.
[138] T. Zhang, Q. Wang, Y. Sun, J. Li, G. Liu, Green Energy Environ. 10 (2025) 1543–1550.
[139] Z.Y. Xiong, W. Hong, Y.Q. Zhao, W.J. Yin, Y. Xu, Appl. Phys. Lett. 126 (2025) 033901.
[140] H.A. Alhadidi Almheiri, N. Singh, D. Shetty, K. Polychronopoulou, A.A. Alhammadi, J. Mater. Chem. A 12 (2024) 7058–7066.
[141] H. Liang, A. Li, N. Yuan, Adv. Powder Mater. 5 (2026) 100370.
[142] Y. Zhu, H. Ji, T. Huang, Y. Sun, H. Pang, Adv. Sustain. Syst. 8 (2024) 2400225.
[143] Y. Cheng, Y. Song, Y. Zhang, Phys. Chem. Chem. Phys. 22 (2020) 6772–6782.
[144] Y. Zhu, S. Murali, W. Cai, et al., Adv. Mater. 22 (2010) 3906–3924.
[145] T. Tang, Z. Wang, J. Guan, Coord. Chem. Rev. 492 (2023) 215288.
[146] Y. Fu, Y. Liao, P. Li, et al., Coord. Chem. Rev. 460 (2022) 214468.
[147] L.N. Zhang, M.Q. Jia, Q.F. Wang, et al., Chin. Chem. Lett. (2026), doi:10.1016/j.cclet.2026.112380.
[148] Y. Yang, L. Zhang, Z. Hu, et al., Angew. Chem. Int. Ed. 59 (2020) 4525–4531.
[149] Y. Anjali, R. Rajeev, B. Manoj, T. Cherian, A. Varghese, Top. Curr. Chem. 383 (2025) 41.
[150] D.S. Teja, B.S. Mallik, Phys. Chem. Chem. Phys. 27 (2025) 11221–11233.
[151] Y. Song, T. Wang, J. Sun, et al., ACS Sustain. Chem. Eng. 7 (2019) 14368–14372.
[152] Z. Song, Y. Liu, J. Zhao, et al., Chem. Eng. J. 434 (2022) 134636.
[153] M. Yan, L. Jasin Arachchige, A. Dong, et al., Inorg. Chem. 60 (2021) 18314–18324.
[154] S. Wang, Y. Zhou, H. Fang, et al., Chin. Chem. Lett. 36 (2025) 110476.
[155] X. Yu, P. Han, Z. Wei, et al., Joule 2 (2018) 1610–1622.
[156] T. Wu, X. Li, X. Zhu, et al., Chem. Commun. 56 (2020) 1831–1834.
[157] Y. Zhao, S. Zhang, C. Han, et al., Chem. Eng. J. 468 (2023) 143517.
[158] M. Xu, Y. Ji, Y. Qin, H. Dong, Y. Li, J. Mater. Chem. A 12 (2024) 28046–28055.
[159] R. Zhu, H. Wang, J. Yu, et al., Sep. Purif. Technol. 364 (2025) 132540.
[160] P. Kumar, G. Singh, X. Guan, et al., Chem. Soc. Rev. 52 (2023) 7602–7664.
[161] W. Lin, S. Yao, H. Chen, et al., J. Energy Chem. 53 (2021) 109–115.
[162] K. Chu, Y. Liu, Y. Li, Y. Guo, Y. Tian, ACS Appl. Mater. Interfaces 12 (2020) 7081–7090.
[163] M. Jiang, Y. Zhu, X. Zhong, et al., Chem. Eng. J. 466 (2023) 143256.
[164] K. Chu, Q. Li, Y. Liu, J. Wang, Y. Cheng, Appl. Catal. B: Environ. 267 (2020) 118693.
[165] N. He, G. Guo, S. Chen, et al., J. Alloys Compd. 1008 (2024) 176766.
[166] Y. Huang, T. Yang, L. Yang, et al., J. Mater. Chem. A 7 (2019) 15173–15180.
[167] X. Zhao, Z. Yang, A.V. Kuklin, et al., ACS Appl. Mater. Interfaces 12 (2020) 31419–31430.
[168] C. Chen, D. Yan, Y. Wang, et al., Small 15 (2019) 1805029.
[169] X. Lv, W. Wei, F. Li, B. Huang, Y. Dai, Nano Lett. 19 (2019) 6391–6399.
[170] B. Long, J. Chen, S.W. Sharshir, et al., J. Mater. Chem. A 12 (2024) 5606–5625.
[171] J. Wang, M. Shi, G. Yi, J. Meng, Q. Li, Mol. Catal. 511 (2021) 111726.
[172] Z. Liu, M. Zhang, H. Wang, et al., ACS Sustain. Chem. Eng. 8 (2020) 5278–5286.
[173] Y. Li, D. Gao, S. Zhao, et al., Chem. Eng. J. 410 (2021) 128419.
[174] B. Chang, L. Li, D. Shi, et al., Appl. Catal. B: Environ. 283 (2021) 119622.
[175] W. Lin, H. Chen, G. Lin, et al., Angew. Chem. 134 (2022) e202207807.
[176] S. Liu, M. Wang, T. Qian, et al., Nat. Commun. 10 (2019) 3898.
[177] C. Wang, Y.N. Zhao, C.Y. Zhu, et al., J. Mater. Chem. A 8 (2020) 23599–23606.
[178] H. Zhong, M. Wang, M. Ghorbani-Asl, et al., J. Am. Chem. Soc. 143 (2021) 19992–20000.
[179] H. He, H. Wen, H. Li, et al., Adv. Sci. 10 (2023) 2206933.
[180] J. Wang, Q. Zhu, J. Wang, et al., Angew. Chem. Int. Ed. 64 (2025) e202415208.
[181] Q. Wang, D. Liang, Z. Zhang, et al., Chin. J. Struct. Chem. 44 (2025) 100599.
[182] S. Qiang, F. Wu, J. Yu, Y. Liu, B. Ding, Angew. Chem. Int. Ed. 62 (2023) e202217265.
[183] L. Fan, Q. Yu, J. Chen, et al., Catalysts 12 (2022) 1005.
[184] J. Wu, S. Wang, R. Ji, et al., ACS Nano 18 (2024) 20934–20956.